International Journal of Impact Engineering 202 (2025) 105294

Contents lists available at ScienceDirect

International Journal of Impact Engineering

journal homepage: www.elsevier.com/locate/ijimpeng

Multiscale study of the dynamic behaviour of additively manufactured Ti6Al4V cellular metamaterials

Andrea Cardeña [a,b], Rafael Sancho [b], Francisco Gálvez [b], Sergio Perosanz [a], Daniel Barba [a,*]

[a] E.T.S. de Ingeniería Aeronáutica y del Espacio, Universidad Politécnica de Madrid, Plaza Cardenal Cisneros 3, 28040, Madrid, Spain
[b] Dpt. de Ciencia de Materiales, ETSI Caminos, Canales y Puertos, Universidad Politécnica de Madrid, C/ Pf. Aranguren, 3, 28040, Madrid, Spain

ARTICLE INFO

Keywords:
Additive manufacturing
Ti6Al4V
Laser powder bed fusion
Metamaterials
Lattice
Dynamic mechanical properties

ABSTRACT

Additive manufacturing (AM) enables the creation of complex geometries like lattices with tunable mechanical behaviour. This technique is frequently used in a diverse range of alloy systems, including steels, nickel-based superalloys, titanium and aluminium alloys, among others. These materials, combined with intricate designs, are leading to innovative metamaterials for lightweight, energy-efficient components in impact applications. However, gaps remain in understanding the connection between the lattice architecture, the resulting microstructure and processing defects and the mechanical behaviour under dynamic conditions of these cellular materials. . This study investigates the dynamic behaviour of Ti6Al4V BCC lattice structures manufactured by Laser Powder Bed Fusion (LPBF), using a multiscale approach to examine both individual struts and whole lattice structures under high strain rates. The Split Hopkinson Pressure Bar and Direct Impact Hopkinson Pressure Bar are used for dynamic testing, while design variables such as printing orientation and strut diameter are considered. Additional analyses on surface quality, microstructure, and fractography are conducted to correlate with the mechanical performance. Results show that the mechanical properties of individual struts are both dependent on the diameter and orientation, especially the former. Struts with larger diameters exhibit higher ductility, while mid-size struts (1 mm diameter) present the higher peak flow stress. For the lattice structures, the dynamic plastic/crushing stress, the energy absorption and the failure modes are influenced strongly by strut diameter, with a minor impact from printing orientation. Lattices formed by struts with larger diameters exhibit higher plastic/crushing effective stresses, but the optimal energy absorption efficiency is achieved with smaller diameters due to densification. These findings highlight the importance of considering size and orientation in the design of lattice structures for dynamic applications.

1. Introduction

Titanium alloys are widely used in several fields such as biomedical and aerospace due to their excellent combination of properties including high strength-to-weight ratio, its excellent corrosion resistance or biocompatibility. Within this type of alloys, Ti6Al4V presents a unique balance between strength, ductility, high-temperature performance and fracture toughness, among other interesting properties [1]. The excellent mechanical performance of this alloy arises from its microstructure formed by a compound of phases including: α (hexagonal-close-packed (HCP)), β (body-centered-cubic (BCC)) and α' (martensite) [1–3]. With these phases as foundational bricks, humans have historically tailored the Ti6Al4V microstructure by means of heat treatments to satisfity a wide variety of mechanical requirements. However, this versatility comes at a price: the complex understanding of its mechanical behaviour.

While Ti6Al4V has been traditionally manufactured by forging and casting methods, more recently novel techniques such as additive manufacturing (AM) are taking the spotlight. These new manufacturing routes allow the creation of near-net-shape complex geometries and lightweight structures while avoiding the need of expensive post-processing tooling and material waste [3–5]. For example, in the biomedical field, AM enables the creation of patient-specific titanium implants and porous scaffolds that promote tissue integration and regeneration, producing structures with customized pore sizes and shapes adapted to each specific function. In high-performance fields such as aerospace or transport, AM allows to maximize the optimization of the parts by reducing and tuning their weight and mechanical behaviour [5–7]. Within the metallic AM techniques, laser powder bed fusion (LPBF) is one of the most used technologies due to its capability

* Corresponding author.
E-mail address: daniel.barba@upm.es (D. Barba).

https://doi.org/10.1016/j.ijimpeng.2025.105294

Available online 18 March 2025

to produce low defect, high performance metallic parts. In the LPBF process, a laser beam selectively melts the regions of a powder bed corresponding to the part geometry, layer by layer. This process follows a pre-designed and sliced CAD model, enabling precise fabrication of complex parts.

In Ti6Al4V, LPBF has been used to produce parts and complex structures [8–10]. Under quasi-static conditions, it is well known that LPBF Ti6Al4V exhibits unique mechanical responses compared to its cast or forged counterparts due to its distinct microstructure formed during the rapid cooling of the LPBF process. This microstructure, primarily consisting of fine acicular martensite (α') from the initial β phase, provides enhanced strength but reduced ductility, a balance that can be further tuned by post-processing methods like heat treatments [6,7]. Two commercial variants of Ti6Al4V powders are commonly used in LPBF: Grade 5 (Ti6Al4V) and Extra Low Interstitial (ELI) Grade 23. While both share a nearly identical chemical composition, Grade 23 has lower levels of interstitial elements (oxygen, nitrogen, and iron), resulting in enhanced ductility and fracture toughness compared to Grade 5. These interesting features and the fact that Grade 23 presents a better biocompatibility makes it a great material for aerospace, automotive and biomedical applications [11].

Regarding the quasi-static properties of LPBF Ti6Al4V, June et al. [12] studied the effects of thickness, geometry, and temperature on the mechanical behaviour of LPBF Grade 23 Ti6Al4V and found that size effects become more pronounced at higher temperatures, with strain hardening increasing due to slip system activation. Moreover, an extensive analysis by Casata et al. [13] analysed the effects of strut size, orientation, and printing parameters of LPBF Grade 23 Ti6Al4V on the static mechanical properties of single struts, revealing that smaller diameters show a reduced elongation due to increased roughness and defects, while horizontal orientations lower strength and ductility due to dross formation. They also noted that process parameters influence mechanical performance based on strut inclination.

The right printing parameters such as printing strategy, energy input, laser velocity layer thickness and many others, widely studied in the literature, allow to manufacture near-to-fully dense parts with very low porosity and defects, as Singla et al. [14] have gathered in their extensive review. For example, Gong et al. [15] observed when studying LPBF Grade 23 Ti6Al4V that too low energy inputs lead to incomplete melting of the powder and the generation of voids or pores. They also noted that defects under 1% are harmless regarding the mechanical properties. In another study, Thijs et al. [16] observed also in LPBF ELI (Grade 23) Ti6Al4V that by increasing the energy density by lowering the hatch spacing or the scanning speed, the volume of Ti_3Al precipitates increases, leading to a higher micro Vickers hardness.

Ti6Al4V AM parts used in the aerospace or marine fields can also be subjected to high-strain loading conditions such as bird strikes, space debris or even be used in energy absorption cases for protective applications and ballistic defense [17–19]. Regarding this, although great efforts have been put in understanding the effect of processing conditions and microstructure on the static properties of LPBF Ti6Al4V, as shown in the previously cited studies, its dynamic mechanical behaviour is a more unexplored domain, as Alkhatib et al. [20] state in their extensive review about dynamic behaviour of light metallic alloys. The dynamic properties of LPBF Ti6Al4V are influenced by factors like strain rate sensitivity, temperature conditions and printing orientation. For example, Yuan et al. [17] found that Ti6Al4V produced by LPBF exhibited a strong strain rate sensitivity regardless of the printing orientation, with the yield stress and flow stress increasing by up to 35% and 55% respectively at high strain rates (1000–4000 s^{-1}) compared to quasi-static conditions. Furthermore, Liu et al. [18] found that the dynamic compressive properties of LPBF Ti6Al4V are strongly influenced not only by strain rate, but also temperature. They showed that, with elevated temperatures, plastic flow and fracture strain are enhanced, facilitating adiabatic shear band formation and dynamic recrystallization, while lower temperatures and strain rates promote strain hardening and limited plastic deformation. Additionally, Yang et al. [19] analysed the effect of the heat treatment in LPBF Ti6Al4V under dynamic conditions and concluded that, although the heat treatment reduced the UTS and yield strength, both of them were increased as the strain rate increased, showing an important strain rate sensitivity. Zhicong et al. [21] studied the effect of scanning speed, printing orientation and strain rate on the dynamic mechanical behaviour of LPBF Ti6Al4V. They found that strain hardening, energy absorption and failure mode depends strongly on those variables, with optimal properties observed at a laser scan speed of 1.2 m/s. They also found that the ultimate flow stress and the energy absorption increased as the building angle increased, with only the samples printing at 45° presenting a shearing fracture pattern. They also observed that higher strain rates produced and enhancement of the strength produced by an intenser dislocation activity.

Furthermore, the work of Cui et al. [22] studied the effect of different levels of porosity in the dynamic response of LPBF Grade 5 Ti6Al4V by using different printing parameters, finding that lower porosity samples exhibit better tensile strength, while porous samples excel in energy absorption. Shock-recovery tests showed that void collapse and energy absorption occur during the impact stage in porous samples, and cracks mainly originate from widely distributed voids. While it is clear that LPBF Ti6Al4V generally show improved strength and strain rate sensitivity, some challenges remain in optimizing their performance, especially in critical load-bearing or impact-resisting roles, needing ongoing research to fully characterize their dynamic response.

On top of this, cellular materials such as lattice structures have attracted the attention of the scientific community due to their unique combination of light-weight designs and customizable structural properties that can be applied in a wide variety of sectors such as satellites and aircrafts [23–26], automotive [27], biomedical [28] or impact protection [29]. These structures are defined as 3D printed periodic, customizable and complex architectures composed of repeating cellular units or random distributed structures, see Fig. 1. There are several classifications in the literature depending on their mechanical response (bending or stretch dominated), morphology (strut or surface based), geometrical distribution (stochastic, non-stochastic), etc [30,31]. For the case of non-stochastic or periodic lattices, Pei et al. [32] includes a complete classification of these materials divided into strut-based (periodic array of struts connected by nodes), shell-based (periodic array of plates folded in a certain way) and Triply Periodic Minimal Surfaces (TPMS), composed of infinite, non-self-intersecting, periodic surfaces. Special attention takes the strut-based periodic lattices due to its simplicity and demonstrated versatility [33–37]. Regarding their quasi-static properties, Wauthle et al. [38] studied the effect of the printing orientation and heat treatment in LPBF Grade 5 Ti6Al4V diamond lattice structures and found that horizontal struts were poorly printed due to the quantity of defects present. They also noted that the trends of the several heat treatments they tested were the same for all building orientations. Choy et al. [39] studied the properties of LPBF Grade 23 Ti6Al4V cubic and honeycomb lattice structures with different strut diameter and orientation. They showed that compressive strength was higher in designs with vertical struts and smaller angles, the orientation affecting the collapsing behaviour.

These AM structures are raising the interest in blast and impact protection applications for their excellent impact energy absorption due to their large densification capacity, high strength and the ability to maintain a constant plateau stress during high deformations [40,41]. The work of Harris et al. [42] using LPBF stainless steel shows that these structures are able to dissipate the kinetic energy at minimum weight while preventing the application of the highest stresses on the protected object. In another work, Calladine et al. [43] shows the importance of the choice of topology, cell size and cell wall material in the dynamic compressive strength and the collapse mode up to the densification strain. The compressive response is also influenced by the strain rate sensitivity of the base material and inertia effects [43].

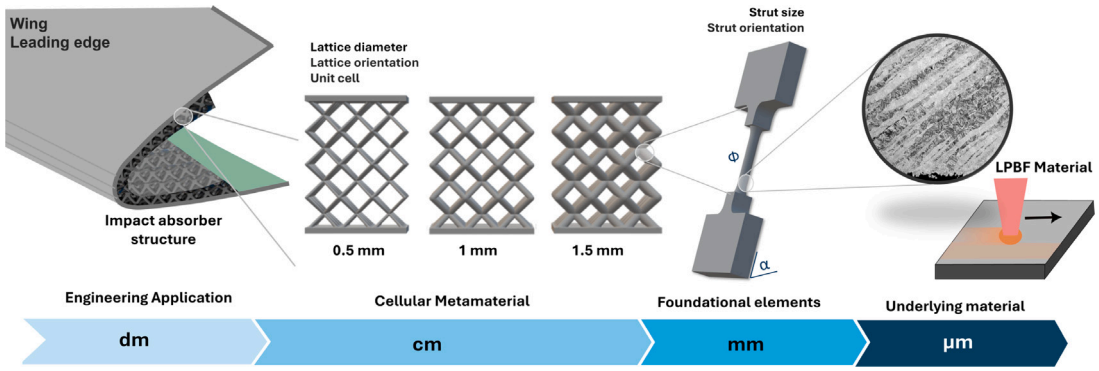

Fig. 1. Dynamic application of AM cellular materials and multiscale approach of the problem.

Moreover, Gangireddy et al. [44] investigated the dynamic mechanical properties of LPBF Ti6Al4V octet lattice structures fabricated via LPBF with varying strut diameters. Their findings indicated that peak strength and energy absorption increased nearly linearly with relative density (strut radius), while the specific values were highest for the smallest strut radius. Cardeña et al. [45] studied the dynamic behaviour of LPBF Grade 23 Ti6Al4V BCC lattice structures with two different diameters and the effect of a standard heat treatment in the properties. While the heat treatment had no significant impact on mechanical properties, the study revealed high strain rate sensitivity compared to quasi-static tests and a greater maximum strain in the lower relative density samples. In another similar study, Merkt et al. [46] tested LPBF Ti6Al4V cubic lattices at different strain rates and found a significant strain rate sensitivity, with the UTS increasing by approximately 20% at higher strain rates. While the decrease in strain to failure was minimal, plateau stress showed a substantial rise between 10%–60% strain, resulting in significantly higher energy absorption at the maximum strain rate of 5 m/s. Additionally, Xiao et al. [47] analysed the energy absorption capabilities of functionally graded LPBF Ti6Al4V lattices with different density gradients subjected to static and dynamic loadings, finding that graded lattice structures have higher specific strength and energy absorption (SEA) than uniform lattices. They also indicated that localization of bending and fracture of the struts in the low density areas were responsible for the overall failure of the graded samples, with no apparent localization in high density areas.

It is clear from the cited literature that, although great research efforts have been done in the fundamental understanding of the static mechanical behaviour of Ti6Al4V LPBF cellular strut-based metamaterials, much less work has been dedicated to their dynamic behaviour. Therefore, there is an incipient need for a fundamental understanding of the effect of the design processing conditions, such as the printing orientation and the size of the metamaterial, on the dynamic mechanical performance of cellular structures. In this work, we aim to address this paradigm by adopting a multiscale perspective on the problem. To do so, the dynamic behaviour and energy absorption of Ti6Al4V Grade 23 BCC strut-based lattice metamaterials manufactured by LPBF are analysed, connecting the cellular behaviour with their inner strut counterparts. With this purpose, first the dynamic behaviour of the individual struts is studied from a fundamental perspective, understanding the effect of geometry and orientation on the defects and microstructure. Then, this understanding is scaled up into the study of the dynamic behaviour of lattice structures composed of the elemental struts studied in the first part of the study. The main objective of the study, shown in Fig. 1, is to find a correlation between the behaviour of the higher-scale cellular structure and the lower-scale individual struts by analysing factors such as size effect, printing orientation and mechanical performance.

This paper is structured as follows: first, in Section 2, the manufacturing conditions, design of the specimens, material characterization and experimental setup are explained; then Section 3 starts with the study focused on the analysis of the lower-scale elemental struts and followed by scaling it up to the analysis of the dynamic behaviour of lattice cellular structures composed of the elemental struts studied in the first part; finally some arising conclusions are drawn.

Table 1
Ti6Al4V powder composition.

Element	Ti	Al	V	Fe	O	C	N	H	Y
Mass (%)	Bal.	6.3	4.0	0.21	0.09	≤ 0.01	0.01	0.001	≤ 0.001

2. Material and methodology

This section outlines the experimental methodology employed in this study, along with a detailed description and justification of its design.

2.1. Material

The base material for this study is Ti6Al4V (Grade 23) ELI powder supplied by Carpenter Additive®. The supplied powder is assured a nominal particle distribution from 14.9 μm (D10) to 53.6 μm (D90). The powder composition provided by the supplier is shown in Table 1.

2.2. Design of the study

The main aim of the study is to address the fundamental effect of the printing orientation and the relative density on the dynamic behaviour of cellular strut-based metamaterials and their foundational struts. To do so, two main sample geometries were studied: (1) single strut dog-bone specimens and (2) BCC cellular metamaterials (see Fig. 2).

Lower scale - Elemental struts:

Dog bone samples resembling the foundational elements of a strut-based cellular material have been manufactured and tested (see Fig. 2, upper part). The gauge length of the specimens is set to 5 mm. Different strut diameters and printing orientations have been selected:

- Strut diameters: three different diameters were chosen based on previous studies in the literature [5,48,49]: 0.5 mm, 1 mm and 1.5 mm. These diameters cover a wide range of scales corresponding to different fields and applications, from biomedical to aerospace. The use of different diameters enables the analysis of possible size effects on the mechanical performance of LPBF Ti6Al4V.
- Strut orientation: struts are printed with angles of 90° (vertical), 55°, 36° and 20° relative to the build plate. Horizontal struts are avoided due to well-known bad printability in terms of roughness and mechanical properties [13,50]. The selected orientation

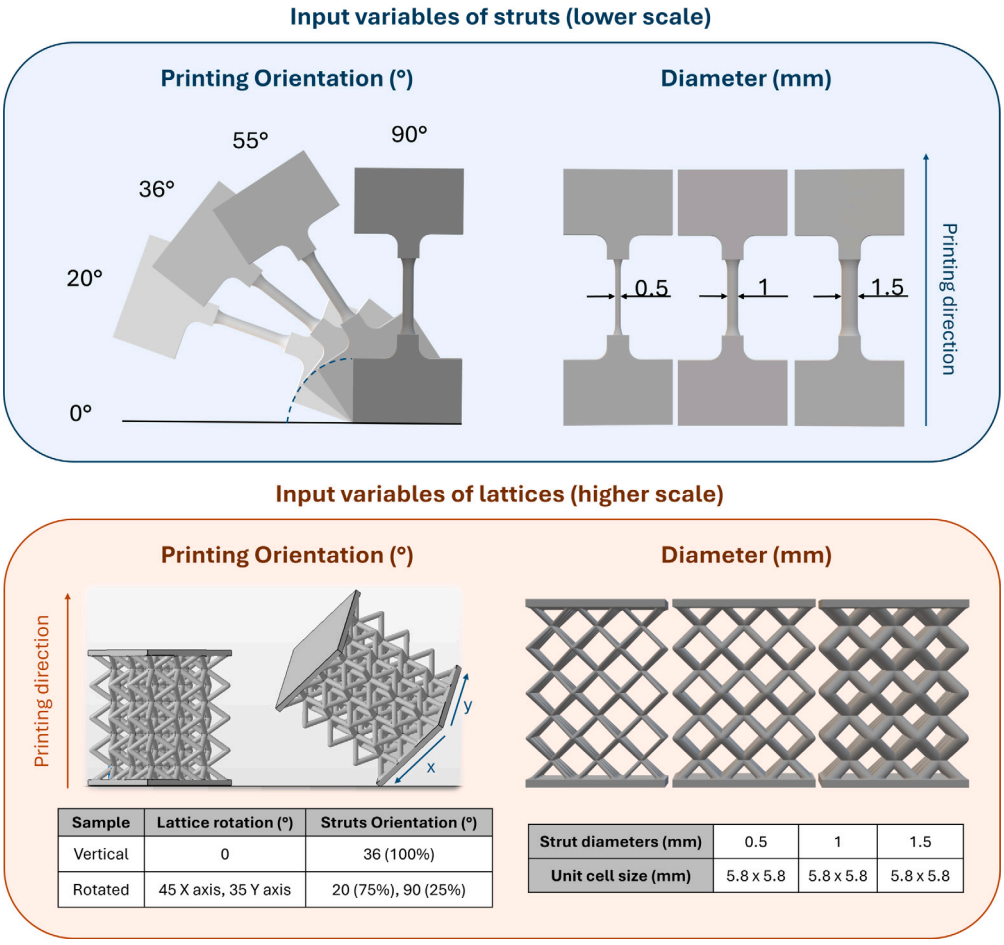

Fig. 2. Variables in the design of single struts and BCC lattices. While gauge length is maintained constant, the printing orientation and diameter is changed to analyse the effect in the surface quality, defects and mechanical performance.

range covers a wide spectrum of angles seen in the most common strut-based unit cells used for printed metamaterials in the literature [51–53].

Higher scale - Cellular materials:

The unit cell geometry chosen for this study was BCC due to its simplicity and the absence of horizontal struts. The length of the lattice's struts is fixed at 5 mm for a direct comparison with the single strut study, giving a unit cell size of approximately 5.8 mm. The tested specimens are composed of 3x4 unit cells, in a compromise solution between addressing the homogenized behaviour of the cellular material and the compatibility with the testing set up. Similarly to the foundational strut study, different diameters and orientations of the cellular lattices are analysed:

- Lattice diameter: the strut diameters of the BCC lattice were set to 0.5 mm, 1 mm and 1.5 mm allowing for a direct correlation with the previous fundamental strut study.
- Printing orientation of the Lattice: the lattice has been rotated accordingly to get a similar range of struts angles as in the fundamental strut study, allowing for direct correlation. With this in mind, vertically oriented and rotated lattices were printed as indicated in Fig. 2. For the case of the vertical lattice, all the struts are aproximately oriented at 36° relative to the build plate. For the rotated lattice (rotated 45° in the X axis and 35° in the Y axis), the struts are printed at 90° and 20° with respect to the build plate.

Table 2
Processing parameters used to produce the Ti6Al4V samples.

	Hatching	Contour
Layer thickness	30 μm	30 μm
Laser Power	129 W	170 W
Scan Speed	1001 mm/s	1600 mm/s
Hatch Distance	73.8 μm	80 μm

2.3. Manufacturing conditions

All the Ti6Al4V specimens cited in the previous section were manufactured by Laser Powder Bed Fusion (LPBF) in an Aconity Mini (Aconity GmbH, Germany) equipped with a 400 W infrared laser. The printing parameters were maintained constant for all the samples and can be found in Table 2. All the samples were printed using a Gaussian laser beam with a spot size of 80 μm and a layer thickness of 30 μm. A stripe hatch-contour scan strategy was chosen, with a 67° rotation after each layer. These parameters were optimized for this alloy to reach a minimum value of porosity. The porosity of the strut samples was analysed to assure the overall value remains below 1%, in accordance to other studies [13,54].

During printing, the inner chamber was protected with an argon atmosphere obtained by a constant flow of the gas. It was ensured that the oxygen concentration remained below 200 ppm throughout the entire process. The base plate used to print the samples is made of Ti6Al4V. Supports were placed in the grip region for the case of the single struts and below the base plates for the case of the lattices. No supports were placed in the gauge length of any of the struts in order to

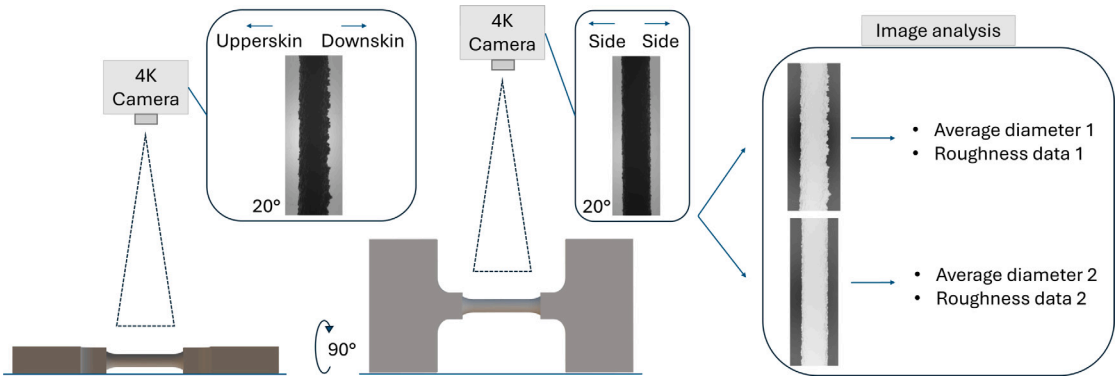

Fig. 3. Methodology followed to capture longitudinal images of the single struts. The two perspectives of the same samples are used for the analysis of the real average diameters and the surface roughness.

resemble as much as possible the conditions of the fundamental struts when they are printed as part of a complete lattice structure.

After printing, the samples underwent a heat treatment at 800° C for 4 h under vacuum, promoting stress relief and the formation of a lamellar $\alpha + \beta$ microstructure.

2.4. Material characterization

2.4.1. Analysis of the real diameter and surface roughness

Before testing each strut sample, longitudinal images of the gauge length were taken using a FLIR camera model Blackfly S USB3, getting images of the area of interest with a resolution in the range of 800x2100 pixels. Two images per strut were captured, rotated 90° from each other (as illustrated in Fig. 3), in order to analyse the sample diameters and the surface roughness. One of the images contains information of the upperskin and downskin profiles while the other image captures the printing side profiles.

2.4.2. Fractography analysis

Fracture surfaces of the struts for each tested condition (orientation and diameter) were analysed using a Hitachi S-3400N scanning electron microscope (SEM) equipped with back-scattered diffraction sensor. Images were taken at an accelerating voltage of 10KV and a magnification of x55, x70, x140 (for the global strut image depending on the diameter) and x700 (for the zoomed images of the centre of the struts) to analyse the fracture in detail. The population of dimples was characterized using ImageJ software [55] to extract the diameter distribution of them. The average length of the dimples was numerically measured by selecting 150 to 200 random length measurements of different dimples for each testing condition. These random measurements were ensured to be representative of all visible dimples in each image.

2.4.3. Microstructural analysis

Once tested, one strut from each orientation and diameter condition was embedded in epoxy resin and prepared in order to analyse the microstructure. The samples were grinded and polished to achieve a mirror-like surface, starting with a 1200-grit abrasive paper, following a polishing using 9 μm to 3 μm diamond suspension and perfecting the final mirror surface using silica suspension solution mixed with H2O2 (70:30). To reveal the microstructure, the surface was etched using Kroll's reagent (1.9% HF, 3.8% HNO_3 and 94.3% H_2O). Microstructural images were acquired at x3.5 and x7 with an Olympus GX53 optical microscope.

2.4.4. Lattice relative density analysis

The experimental relative density of the BCC lattices has been measured for each condition (diameter and orientation) in order to assess its deviation from the intended designed one. To do so, the lattices were weighted and measured, and their relative density was calculated following:

$$\rho_r(\%) = \frac{W_{lattice}/\rho_{Ti6Al4V}}{V_{boundingbox}} \cdot 100 \quad (1)$$

where $W_{lattice}$ and $V_{boundingbox}$ are the weight of each sample and the volume of the bounding box occupied by the BCC lattice respectively, and $\rho_{Ti6Al4V}$ is the bulk density of Ti6Al4V (4.43 g/cm^3). $W_{lattice}$ is calculated by substracting the weight of the plates from the total weight of the specimen. The $V_{boundingbox}$ is calculated from measurement of the bounding box containing the BCC lattice.

2.5. Mechanical testing

Given the multiscale nature of this study, two different experimental set-ups based on the Hopkinson bar theory [56] were employed for the mechanical characterization of the single struts and the lattice metamaterials. This was necessary due to the differences in the sample dimensions and their structural impedance.[1] All the specimens were tested at room temperature.

2.5.1. Struts: miniaturized Split Hopkinson Tensile Bar (SHTB)

Dynamic tensile tests on single struts were conducted using a Split Hopkinson Tensile Bar (SHTB) setup, as illustrated in Fig. 4. The setup was constructed from 10 mm diameter Al7075 T6 aluminium bars for both the incident and transmitted bars, with an aluminium tube used as the proyectile. In this configuration, the single-strut specimen was mounted between the bars using an auxiliary coupling system.

The coupling system consists of two main components: an adapter part made of the same material as the bar (Aluminium 7075-T6) attached to the testing bar with a headless M6 screw on one side and glued to the specimen itself on the other side. A detailed representation of the grip system geometry is provided in Fig. 4.

This coupling system was custom-machined in the laboratory to meet the specific requirements of the experimental setup. This design ensures continuous contact among the bar, screw, and adapter, avoiding unwanted reflections of the stress wave and maintaining the impedance consistency of the overall system. The adhesive used for bonding the adapter to the specimen is a high-performance epoxy resin (Loctite EA 9466), selected for its ability to withstand the anticipated maximum shear stresses and impact loads during testing. To ensure

[1] Structural impedance = $\rho c A$, being A the cross-sectional area, c the wave speed in the material and ρ the density.

homogeneous impedance across the testing system, all components are fabricated from the same material as the bars (Aluminum 7075-T6) and maintain an identical cross-sectional area.

The tensile pulse is initiated by launching the striker, with compressed air, against the anvil end of the incident bar, generating a tensile stress wave that travels along the length of the bar. Upon reaching the interface between the bar and the specimen, the wave is partially reflected and partially transmitted to the second bar throughout the specimen.

Strain measurements were performed using a full Wheatstone bridge with two rosettes of Vishay micromeasurements CEA-06-125-UT-350 type gauges, with two longitudinal and two transverse gauges relative to the bars, to compensate for bending and maximize the gain. The signal conditioning system used was a Vishay 2200, with no filtering applied.

The gauges were located at 200 cm (input bar) and 50 cm (output bar) from the bar-specimen interface. By measuring and recording the voltage signals for each strain gage, the incident (ε_i), reflected (ε_r), and transmitted (ε_t) strain waves can be extracted. By applying one-dimensional elastic wave propagation theory, the engineering strain rate ($\dot{\varepsilon}$), engineering strain (ε) and engineering stress (σ) can be calculated using the following equations:

$$\dot{\varepsilon} = -\frac{2c_{bar}}{l_0}\varepsilon_r \tag{2}$$

$$\varepsilon = -\frac{2c_{bar}}{l_0}\int \varepsilon_r dt \tag{3}$$

$$\sigma = \frac{E_{bar}A_{bar}}{A_0}\varepsilon_t \approx \frac{E_{bar}A_{bar}}{A_0}(\varepsilon_i + \varepsilon_r) \tag{4}$$

where c_{bar} is the sound velocity of the bar material, l_0 and A_0 are the initial gauge length and the cross-sectional area of the specimen and E_{bar} and A_{bar} are the elastic modulus and cross-sectional area of the bar, respectively. Furthermore, a Phantom Veo 710 high-speed camera was used to capture the specimen's deformation during testing with a resolution of 256 × 64 pixels and a frame rate of 260 000 fps. The displacement was quantified using Digital Image Correlation (DIC) techniques, providing an additional and more accurate measure of longitudinal strain and deformation in the strut specimen.

In order to align the strain rate with that obtained from the lattices across all struts, an initial calibration of the bar was conducted. During the calibration, the correct input pressure for each condition (diameter and orientation) was fixed to assure that all the struts were subjected to 900 s^{-1}–1000 s^{-1}, the same order of magnitude as the lattices and the minimum that could be reached with the bar.

2.5.2. Lattices: direct impact Hopkinson pressure bar (DIHPB)

The lattice specimens were tested using a Direct Impact Hopkinson Pressure Bar setup as illustrated in Fig. 4 to evaluate their compressive properties under dynamic loading while ensuring densification, an essential condition for assessing energy absorption behaviour.

The DIHPB configuration was chosen over the conventional Split Hopkinson Pressure Bar (SHPB) primarily to achieve lattice densification. In the conventional SHPB, the maximum strain in the sample is constrained by two factors: (1) the projectile velocity and (2) the length of the projectile.

The maximum striker velocity may be limited by the acceleration mechanism of the set-up, but more importantly, it is constrained by the yield strength of the incident bar material. When testing low-impedance materials, the magnitude of the reflected strain (ε_r) tends to be similar to the magnitude of incident strain (ε_i) due to the impedance mismatch between the incident bar and the specimen. If a material with low Young's modulus, such as aluminium, is chosen for the incident bar to improve signal resolution, the maximum striker velocity is further constrained to prevent yielding on the incident bar. Conversely, selecting a material with a high yield strength (and consequently a high Young's modulus) to avoid yielding reduces the signal resolution when subtracting the incident and reflected waves to compute the force at the incident-specimen interface.

With regard to the projectile length, increasing its length is not always feasible due to physical constraints of the equipment and the cannon. Additionally, the accuracy of force calculations in the incident bar may be compromised by wave dispersion. Longer projectiles necessitate placing strain gauges farther from the ends of the incident bar to avoid wave superposition, which can distort the measurements. For these reasons, many researchers opt to use Direct Impact Hopkinson Pressure Bar for testing lattice or cellular materials [41,57–59].

Taking into account the previous argumentation and the low impedance of lattice metamaterials, the experimental set-up, which is illustrated in Fig. 4, consisted of a VascoMax-C250 projectile with a length of 1.2 m and a diameter of 25.4 mm, and a Al7075 T6 output bar of 25.4 mm diameter and 4 m length. In all cases, the projectile velocity was, approximately 13 m/s, resulting in a strain rate between 500–600 s^{-1}.

For all the lattice samples, although the printing orientation changes, the BCC unit cells forming the lattice present the same direction with respect to the loading axis. The tests were recorded by a high speed camera Phantom Veo 710, at 100 000 fps with 256 × 168 resolution. Displacement and strain information of the samples were extracted by DIC techniques given the fact that, in direct impact configuration, neither the incident wave nor the reflected wave was measured.

Strain measurements were performed using a full Wheatstone bridge with two rosettes of Vishay micromeasurements CEA-06-125-UT-350 type gauges, with two longitudinal and two transverse gauges relative to the bars, to compensate for bending and maximize the gain. The signal conditioning system used was a Vishay 2200, with no filtering applied. The gauges were located at 50 cm from the bar-specimen interface in the output bar. From this signal, it is possible to extract the engineering stress using the equation:

$$\sigma = \frac{E_{bar}A_{bar}}{A_{plate}}\varepsilon_t \tag{5}$$

where A_{plate} is the area of the plate of the lattice and E_{bar} and A_{bar} are the elastic modulus and cross-sectional area of the output bar, respectively.

The drawback of the Direct Impact Hopkinson Pressure Bar setup is the inability to verify force equilibrium, as force data is only available at the distal (non-impacted) face. In this study, force equilibrium, and thus the validity of the data, is assumed based on previous experimental and numerical results from the literature. For instance, Wang et al. [57] reported that closed-cell aluminium foams with relative densities of 10%–14% and a sample length of 32 mm maintained force equilibrium for impacts up to 16 m/s, recording plateau and collapse stresses of 3.49 MPa and 5.35 MPa, respectively. Fila et al. [58], using an Open Hopkinson Bar set-up, obtained forces values at both the proximal and distal faces in tests on auxetic SS316L structures with 0.3 mm strut thickness and specimen dimensions of 12 × 12 × 12.5 mm^3, demonstrating force equilibrium up to striker velocities of 20 m/s. Lastly, Jin et al. [60] provided numerical results on Ti6Al4V BCC lattices with a strut thickness of 0.8 mm, a unit cell size of 5 × 5 mm^2, and a specimen length of 21 mm (comparable to the dimensions in this study), showing force equilibrium up to a relative velocity between faces of 32 m/s. Moreover, the DIC data allowed the authors to estimate the force equilibrium for the 1.5 mm thick-strut specimen. However, force equilibrium could not be explicitly verified for the other two lattice types due to noisy results stemming from measurement uncertainties with DIC. This analysis is summarized in Appendix A.

3. Results and discussion

In this section, the results arising from the study are presented and discussed. First, the lower scale study focused on the fundamental struts is presented. Then, the second part of the section is focused on the mechanical behaviour of the strut-based cellular metamaterials linking their properties to the phenonema observed at the foundational struts.

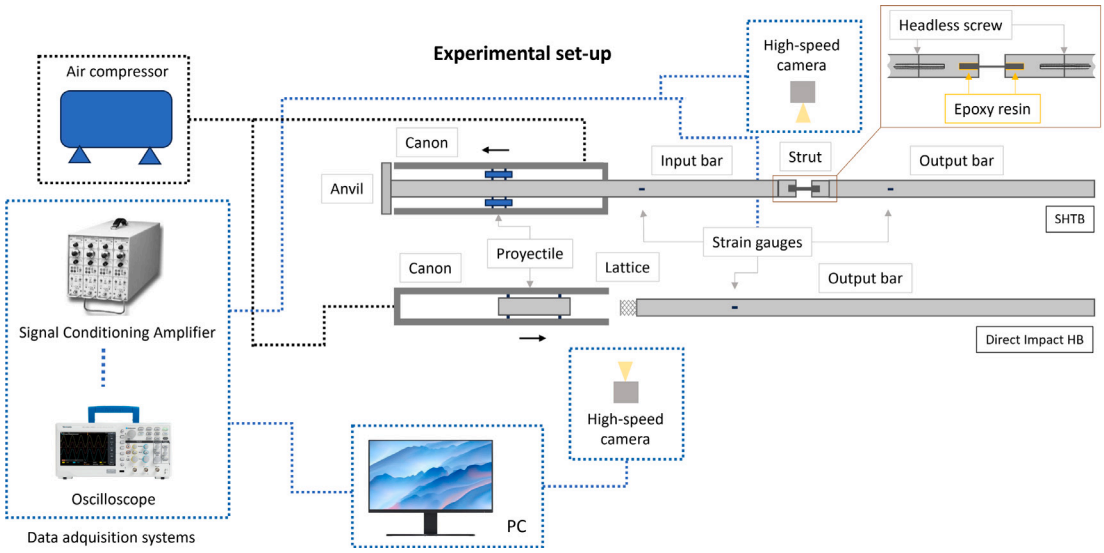

Fig. 4. Schematic of split Hopkinson Tensile Bar (SHTB) and Direct Impact Hopkinson Pressure Bar used for the dynamic characterization of the material.

3.1. Lower scale - Study of elemental struts

3.1.1. Manufacturing accuracy and defect analysis

This section addresses the effect of the strut diameter and orientation on the printing deviation and the presence of defects (*e.g.*, roughness). First, the manufacturing dimensional accuracy is analysed, followed by a quantitative analysis of roughness.

Geometrical accuracy. As a measurement of the dimensional accuracy, the geometrical CAD deviation of a single strut is defined as:

$$\text{CAD Dev} = \frac{A_{\text{real}} - A_{\text{nominal}}}{A_{\text{nominal}}} \cdot 100 \tag{6}$$

where A_{real} is the average area extracted from direct measurements of the struts and A_{nominal} is initial intended area established in the design stage. A_{real} is obtained as:

$$A_{\text{real}} = \pi\left(\frac{D_1 D_2}{4}\right) \tag{7}$$

where D_1 and D_2 are the average real diameters extracted from the two perpendicular images of each strut.

The resulting CAD Dev values are presented in Fig. 5. For each strut condition, the maximum, the average and the minimum diameter measured are indicated. In general, the standard deviation is between 0.15% and 0.93% in all cases, except for the strut of 0.5 mm - 20°, which is 1.51%.

There is a direct correlation between the CAD deviation and the diameter of the struts. As the CAD diameter decreases, the deviation increases drastically, reaching values between 70%–90% for diameters of 0.5 mm. This trend is observed for all the printing orientations. This is in accordance with previous results in the literature. For example, Bregoli et al. [61] observed in LPBF Grade 23 Ti6Al4V that the printing accuracy improved significantly with increasing strut diameter, where larger diameters (0.9 mm) resulted in dimensional deviations being reduced by approximately half compared to thinner struts (0.5 mm). Bartolomeu et al. [62] also found a similar trend and concluded a systematic linear correlation between the CAD and the LPBF parts for wall size of cellular materials. More recently, Casata et al. [13] also noted a decrease in the CAD deviation as the strut diameter increases.

The effect of the printing orientation is much less acute. There is a slight decrease of the printing accuracy as samples are printed more vertically. For the case of 1.5 mm, the deviation decreases less than 10% as the printing angle decreases to the lowest angle. Following the same trend, the deviation of the 1 mm diameter decreases around 15%. It is for the case of the smallest diameter (0.5 mm) when a lower deviation around 26% is appreciated when the orientation angle decreases to its minimum studied value of 20°. Other authors have also studied the influence of printing orientation of the geometry accuracy of LPBF lattices and struts. For example, Dong et al. [51] studied the geometric accuracy of LPBF AlSi10Mg lattices and found an average deviation of 2.9% for the 35.5° struts, a value that decreased to 1.5% for the case of the vertical struts. Cansizoglu et al. [63] studied the printing accuracy of electron beam PBF (EB-PBF) Ti6Al4V lattices and observed that the real diameter was higher for the case of the vertical struts, similar to the trend found in this study. Zhang et al. [64] studied the accuracy of EB-PBF Ti6Al4V struts with different diameters and orientations and found that, for the same diameter, the deviation depending on the printing angle varied slightly, generally decreasing when printed more vertical. They also found that struts between 0.1 mm–1.5 mm diameter are printed oversized, as observed in this study. The different trends observed in the literature can be caused due to the printing accuracy being highly influenced by several factors such as printing parameters, CAD diameter and printing orientation. Moreover, there is a general trend indicating that the printing orientation is the less influential factor in the cited bibliography, in accordance with our results.

Surface roughness. Before testing, the longitudinal roughness was analysed for each strut as a function of its orientation and diameter. The average roughness of the downskin and upperskin were obtained from longitudinal images of the gauge length of each strut by image analysis. Representative examples of these images are presented in Fig. 6.

The quantitative results of the surface roughness (R_a) for the downskin and upperskin are presented in Fig. 7. For consistency, for the case of the 90° struts, downskin and upperskin measurements are indicated although both roughness values correspond to vertical surfaces. As expected, the average roughness of the downskin is higher than the upperskin for all orientations and diameters. This has been found to be related to the different sources causing the roughness in the upperskin and downskin [13,65]. Tian et al. [65] observed two different sources of roughness in LPBF Ti6Al4V struts: one related to the layer by layer nature of the LPBF process (stair-stepping shape along the length of the sample) and another one related to the adhesion of powder particles during melting. For the case of the upperskin, the first one plays a more important role, while the roughness of the down-skin is mainly produced by the second source. This is in agreement with Fig. 6 as it can be observed that for the case of 20°, the staircase type of roughness is present in the upperskin, and partially melted particles are more pronounced in the downskin area. This difference between upperskin

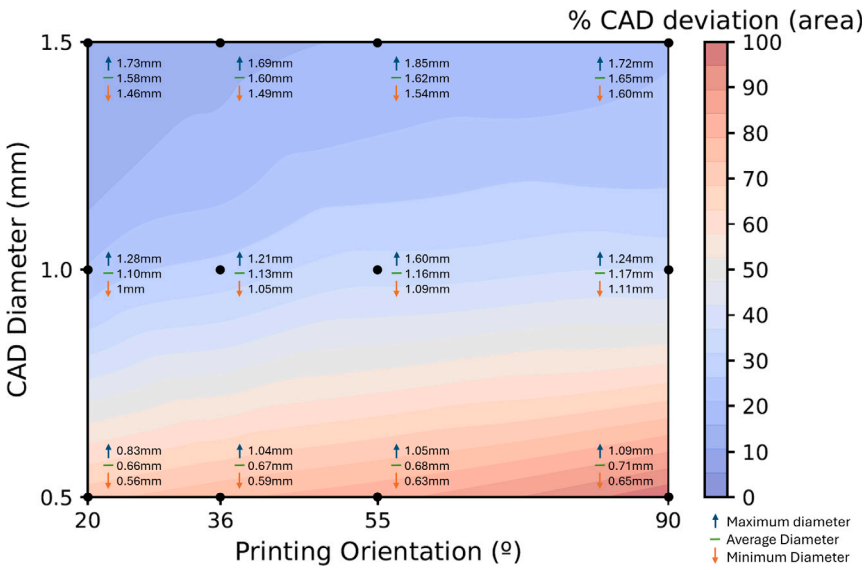

Fig. 5. Measured CAD deviation based on the area of the struts depending on the strut diameter and orientation. The maximum, average and minimum diameter measured for each condition is indicated.

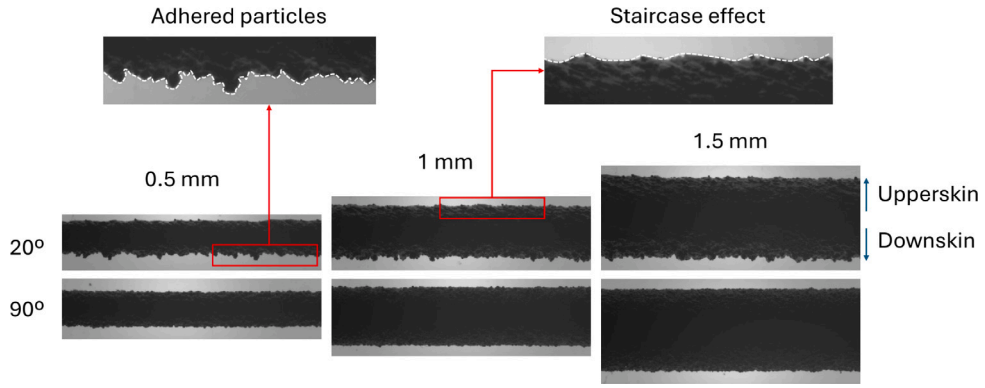

Fig. 6. Images of the struts printed at 20° and 90° (vertical) used for the surface roughness analysis. The downskin is the downward facing surface closest to the buildplate, while the upperskin is the opposite surface, upwards facing.

and downskin is more pronounced as the strut is more tilted, being the downskin roughness approximately twice the upperskin value for the case of the 20° oriented struts, see Fig. 7. This can be caused by the deeper extension of the melt pool toward the powder occurring in more tilted samples, allowing a larger amount of powder to adhere to the downskin [13,65]. The effect of this roughness on the mechanical properties will be further discussed in following sections.

3.1.2. Mechanical behaviour of elemental struts

In this section, the mechanical behaviour of the elemental struts under dynamic conditions is presented. First, the overall results are shown as stress–strain curves, followed by an analysis and discussion of each mechanical property (*e.g.*, failure strain and peak flow stress).

Stress–strain dynamic curves. The engineering stress–strain curves of the elemental struts are presented in Figs. 8 and 9, grouped by diameter and orientation, respectively. It can be observed that in terms of repeatability, the 0.5 mm struts the greater dispersion in the curves. In contrast, the 1 mm and 1.5 mm struts exhibit a higher repeatability, with the curves showing low variability in mechanical behaviour. The significant dispersion observed for the smallest diameter in all cases is potentially caused by the effect of surface defects, particularly critical in high surface-to-volume ratio specimens, such as 0.5 mm struts. This can lead to potentially premature failures and low consistency in the mechanical properties, aligning with previous studies on similar diameters [5,50].

The mechanical behaviour of 0.5 mm struts is characterized by a stress–strain curve that exhibits a bell-shaped configuration. In contrast, struts with larger diameters (1 mm and 1.5 mm) exhibit a different pattern: initially, there is a peak in the flow stress (typical from dynamic tests [66–68]) followed by a plateau or intermediate region, and then a stress collapse phase, where there is a significant and continuous decrease of the load-bearing capacity of the sample due to the effects of adiabatic heating and damage evolution. The presence of the plateau region can be rationalized by considering the competition between strain hardening processes and the thermal softening induced by adiabatic heating, resulting even in some stress oscillations [18,69]. According to the experimental results, the extension of this plateau region is proportional to the diameter size. In this sense, the limit case of the bell-shaped curve for 0.5 mm struts can be elucidated by considering that any defects present, whether they involve internal porosity or are due to surface roughness (see), are likely to be critical due to the high surface-to-volume ratio of the specimens. These defects can more easily progress to a condition where the evolution of damage becomes a predominant factor and the load-bearing capacity collapses.

Ductility. The strain to failure extracted from the stress–strain curves has been plotted in Fig. 10 as a function of the strut size and orientation. When comparing with quasi-static results from the literature

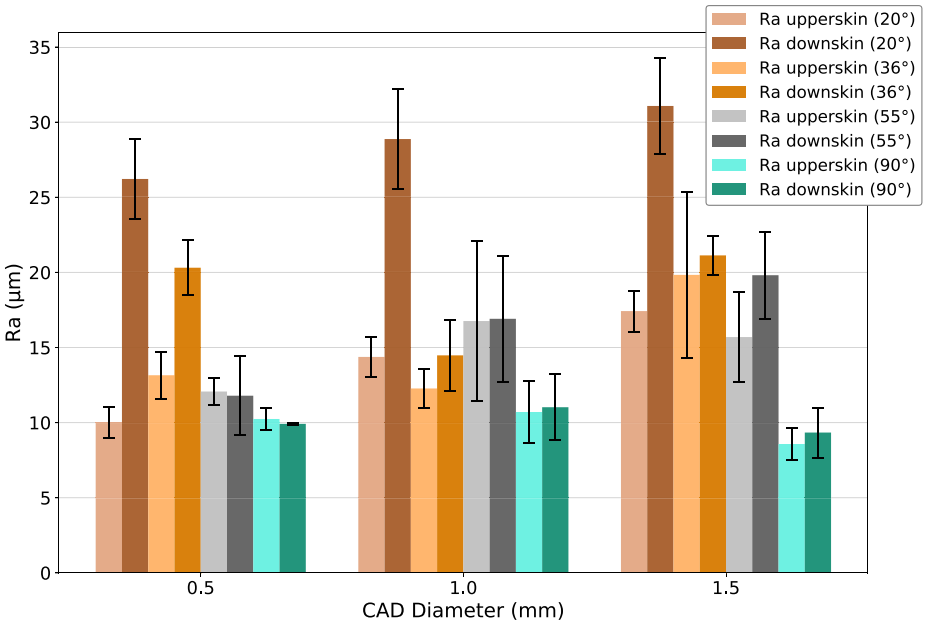

Fig. 7. R_a of the downskin and upperskin of the struts based on diameter and printing orientation. Each colour corresponds to a different orientation, being the darkest tone the R_a of the downskin.

for similar geometries [13], there is a clear trend: higher strain rate results in an increase of the strain to failure. This is specially the case in conditions where the stress plateau region is present (*e.g.*, for 1 mm and 1.5 mm struts). This phenomenon related to the strain rate, which seems to be counterintuitive, has been also observed in previous studies in the literature [66,69]. Dehgahi et al. [69] observed in LPBF maraging steel that the total accumulated strain before failure increased significantly with strain rate. They associated this phenomenon with the higher adiabatic heating effect as the strain rate increases, which can lead to a domination of the thermal softening over the strain hardening in the stress plateau, which eventually extends the plastic region. This phenomenon can explain the increase of ductility observed in Fig. 10 when compared with the quasi-static counterparts.

In terms of the effect of the strut diameter, it can be observed a significant increase in the strain to failure as the diameter increases. The strain to failure raises from 6%–8% at 0.5 mm to 12%–19% at 1.5 mm. As observed in the stress–strain curves in Figs. 8 and 9, this increase is mostly sourced from the higher plastic strain accumulated in the material during the stress plateau region. As indicated in the previous paragraph, two effects coexist in this region: the thermal softening and the strain hardening [69]. This competition can be inferred specially for the case of 1.5 mm, where stress fluctuations in the plateau region can be clearly observed. It can be expected that the thermal softening is strongly affected by the surface-to-volume ratio of the sample, producing a marked size effect. This is because during plastic deformation, a portion of the mechanical energy converts into heat. In dynamic conditions, this heat is accumulated and unable to be dissipated due to the adiabatic nature of rapid loading. For smaller diameters, the dissipation is expected to be higher due to a larger surface-to-volume ratio. This can reduce the thermal softening effect, leading to a predominance of the strain hardening mechanism. It could also promote a faster achievement of higher stress levels at stress concentrators such as manufacturing defects (roughness, pores), which can lead to a premature failure [70]. This can be observed in Fig. 8 where, for the case of 0.5 mm, the plateau region is inexistent, leading directly to a failure of the material, while the plateau region increases as the diameter increases to 1 mm and 1.5 mm. Another factor to take into account is the real effect of these defects as stress concentrators in the material. Although similar roughness values were observed in Fig. 7 for the different diameters, the relative effect on the small struts is expected to be higher (*i.e.*, due to the smaller volume of these samples). Therefore, these defects are expected to have a more detrimental effect for the case of 0.5 mm. Finally, defects and geometrical deviations or heterogeneities can also promote strain localization during deformation. Premature strain localization can lead to lower failure strains. The effect of the geometrical deviations and defects on the stain localization is expected to be higher for smaller samples [71]. These hypotheses are in agreement with the observed results in Figs. 8 and 10.

Another feature to study is the effect of the orientation of strain to failure. As observed in Fig. 9, as the diameter increases from 0.5 to 1 mm, the influence of the orientation on the strain to failure increases. This can be due, as mentioned before, to the higher effect of the manufacturing defects at small strut diameter. In any case, a consistent trend can be observed across all cases: 20° struts show a lower strain to failure, regardless of size. The mechanical performances of the 36°, 55°, and 90° orientations are quite similar, often making them difficult to distinguish in most cases. This behaviour could be directly related to the surface quality and defects, with a higher roughness observed in Fig. 7 for 20° struts, specially in the downskin, which can lead to faster achievement of critical stresses at stress concentrators and therefore, premature failure. The vertical struts printed at 90° present a smoother and more homogeneous surface, with both sides showing practically the same roughness, reducing the potential of premature failures due to the initiation of cracks caused by surface defects, which is in agreement with results observed in Fig. 9.

Peak flow stress. As seen in Fig. 11, the peak flow stress values for different printing orientations vary in their degree of dispersion depending on the strut diameter. The overall peak flow stresses are enclosed in the range of ≈ 1850 and 2200 MPa. For small size diameters (0.5 mm), it can be observed a larger scatter in the values when compared to larger diameters. This can be due to the higher relative effect of defects as stress concentrators for small sized specimens, see Fig. 6, as indicated for the strain to failure. The higher scatter at 20° for the case of 0.5 mm can be due to the higher presence of surface defects at these printing conditions as shown by the roughness results in Fig. 7.

In terms of the effect of the strut diameter, the 1.5 mm diameter consistently exhibits lower average peak flow stress for most orientations, except at 55°. The minimum value of peak flow stress is reached

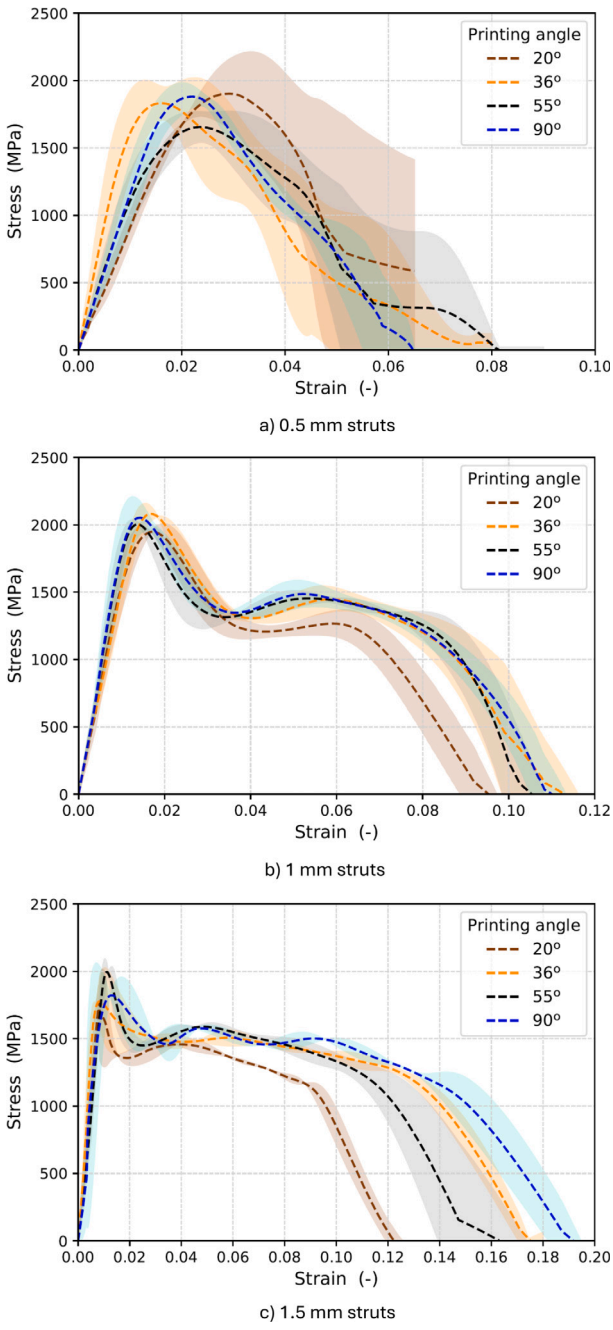

Fig. 8. Engineering stress–strain curves of Ti6Al4V elemental struts as a function of orientation for struts with 0.5 mm, 1 mm and 1.5 mm diameter. Shaded area represents the standard deviation, while the dashed lines indicate the averaged curve from three repeats per condition.

by the biggest diameter (1.5 mm) printed at 36°. Conversely, the 1 mm diameter struts demonstrate the highest overall performance for all orientations, with a consistent maximum stress above 2000 MPa and a peak value of 2136 MPa for the case of 36°. It is important to remark the similarities in the behaviour of 0.5 mm and 1.5 mm diameters, which are very close in performance and below 2000 MPa in most of the cases, being the only exception the 1.5 mm diameter at 55°. As a summary, the peak flow stress present a higher value form mid-size struts (1 mm) decreasing for larger and smaller printing diameters (*i.e.*, 1.5 mm and 0.5 mm) for most orientations.

To the known of the authors, no comparable studies addressing the effect of size in dynamic conditions has been performed for LPBF Ti6Al4V. Nevertheless, results in the literature for quasistatic conditions support the observations presented in Fig. 11 regarding the effect of the strut size. Previous quasi-static results analysed from the literature suggest that UTS decreases with the size of the specimen, but also becomes more repetitive and less sensitive to the printing orientation. Barba et al. [5] concluded a quasi-static UTS window for LPBF Ti6Al4V between 1075 and 1175 MPa for dog-bone specimens printed horizontally and vertically with 0.5×1, 1×2 and 1.5×3 mm^2 gauge area. They found that the UTS increases as the strut print size decreases up to a peak value at around 0.5×1 mm^2 gauge area. At print sizes below this area, the UTS drops, accompanied by a higher scatter. When printing larger strut areas, Simonelli et al. [6] observed working with the same material a consistent UTS around 1050 MPa for vertically and horizontally printed dog-bone tensile bars with a 3x6 mm^2 gauge area, coincident with the lower values presented in [5] for larger struts (3x6 mm^2). The work of Barba et al. [5] also shows that refinement of the microstructure triggered by the printing thermal history at small size specimens might be behind the size-hardening effect when printing small size diameters. These literature observations in quasi-static conditions are in accordance with the observations of this study under dynamic conditions, although with small differences. As the printing size decreases, the thermal history during printing and posterior heat treatment produces finer microstuctures [5]. This can lead to a material with higher flow stresses [5,72] as the printing size decreases, which is observed in Fig. 11 when moving from 1.5 mm to 1.0 mm. However, as size, there is another phenomenon with opposite effect: as the surface-to-volume ratio increases, the effect of surface defects increases, promoting the initiation and propagation of cracks and eventually leading to early failure at lower stress values (which effectively can reduce the peak stress values). This effect is believed to be more prominent at smaller diameters (*i.e.*, 0.5 mm), leading to a drop of strength even though the intrinsic material properties might be higher than for larger diameters, see Fig. 11.

In terms of the strain rate sensitivity of the peak stresses, the results of Fig. 11 show a strong effect of the strain rate on the peak stress when comparing to the UTS at quasi-static conditions from the literature [13,73–76]. The peak stress in dynamic conditions (≈ 1000 s^{-1}) is approximately twice as high as the UTS in quasi-static conditions (10^{-2} s^{-1}). This is in agreement with previous results in the literature for Ti6Al4V. Waymel et al. [73] investigated the effect of strain rate, heat treatment and printing orientation on LPBF Ti6Al4V and found that the yield strength exceeded 2000 MPa when the strain rate reached 5000 s^{-1}, closely aligning with the results obtained in the present study at similar strain rates. It is important to note that this train rate sensitivity is not exclusive to Ti6Al4V manufactured by LPBF. Alaghmandfard et al. [74] showed the strain rate sensitivity of EB-PBF Grade 5 Ti6Al4V by testing with a SHPB vertically and horizontally printed bulk samples at different strain rates. Their results showed a similar trend to the present study with the UTS growing from $\approx$ 1100 MPa at 150 s^{-1} to $\approx$ 2000 MPa at 1300 s^{-1}. This work was further extended to higher strain rates in [75]. In this case, they confirmed the opposite effect of strain rate hardening and strain softening (due to thermal softening) during the dynamic tests. Their results showed an increase of $\approx$ 17% in the UTS from 700 s^{-1} to 2100 s^{-1}. In their study, Nemat-Nasser et al. [76] studied the effect of traditionally manufactured Ti6Al4V microstructure on their dynamic thermomechanical response. Their results present higher UTS values as the test strain rate increases from 10^{-3}s^{-1} to 7000 s^{-1}, with noticeable strain rate and temperature sensitivity observed in all cases.

Interestingly, the dynamic factor in additively manufactured Ti6Al4V is higher than what it is observed in the conventionally manufactured alloy, as we can see a relative increment of the yield stress of around 35% in the work of Nemat-Nasser et al. [76] from quasi-static strain rates to 2000 s^{-}1, while there is an average increment of 100% when analysing the strain rate sensitivity of the previous cited AM Ti6Al4V (taking into account the present work too) if the reference quasi-static

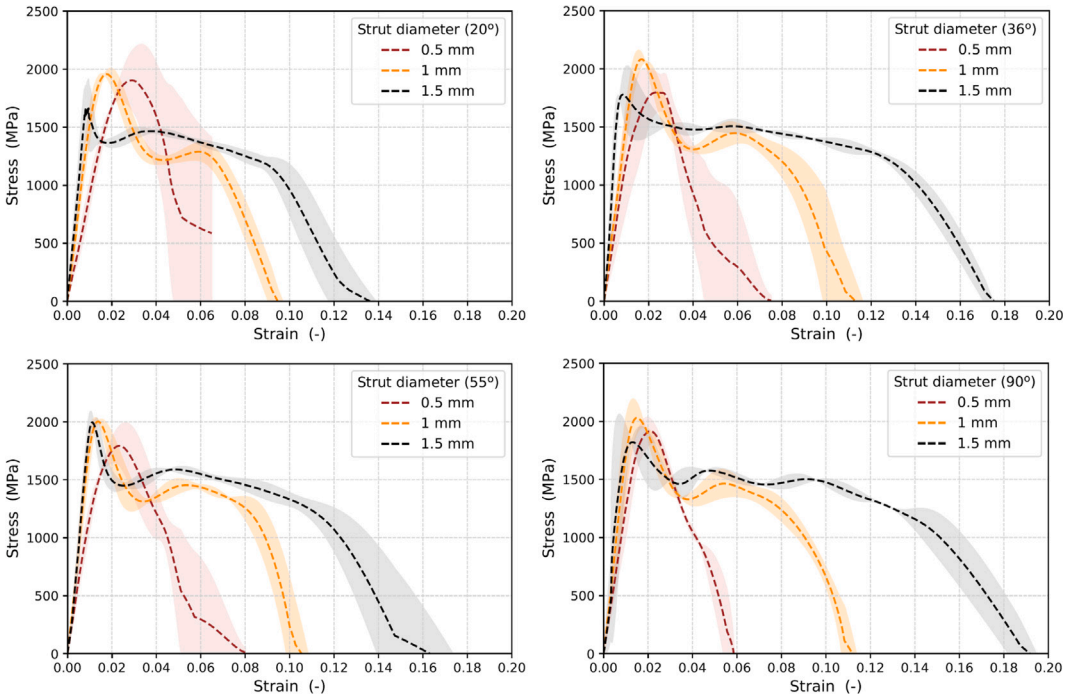

Fig. 9. Engineering stress–strain curves of Ti6Al4V elemental struts as a function of diameter for struts printed vertically (90°), at 55°, at 36° and 20°. Shaded area represents the standard deviation, while the dashed lines indicate the averaged curve from three repeats per condition.

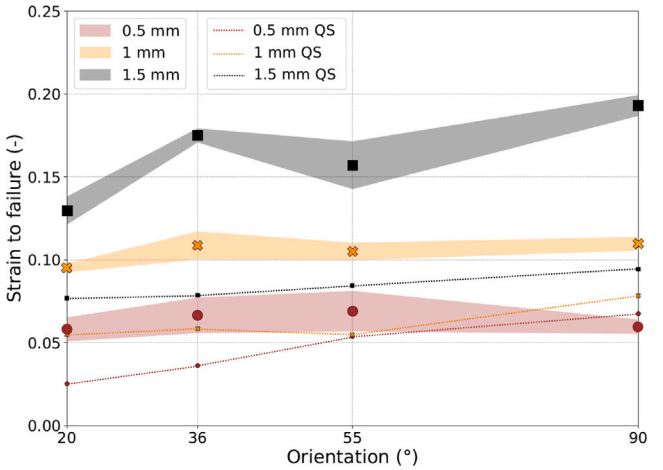

Fig. 10. Average strains to failure as a function of printing orientation and diameter. Distinct symbols and colours represents each strut diameter. Shaded regions indicate the standard deviation of the measurements. Quasi-static (QS) results from the literature [13] are presented for comparison as dashed lines.

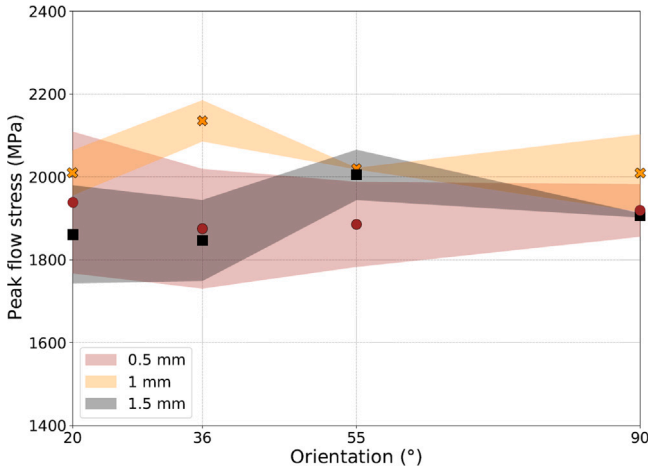

Fig. 11. Peak flow stress as a function of printing orientation and diameter. Distinct colours represents each strut diameter. Shaded regions indicate the standard deviation of the measurements.

value for the yield stress is taken from studies such as the one from Casata et al. [13], which is around 1000 MPa. This can be an effect of the microstructure which will vary from one processing route or another.

3.1.3. Microstructural and fractography analysis

Microstructural analysis. The optical images of the tested samples with different strut orientations and diameters are presented in Fig. 12. In these images, the typical "basket-wave" microstructure of α laths is observed at higher magnification. Interestingly, the primitive β grain structure can be inferred from the different contrast of gray scale. These β grains are the first grains formed as the material cools down from laser melting [77]. Further cooling leads to the formation of martensite plates α' within those β grains, which transform into α' $\rightarrow$ α with subsequent heat treatment. The grain growth of the β follows the heat flux during cooling. In LPBF, the heat flux usually follows the laser direction (vertical) in the bulk region and a more chaotic direction near the surfaces (due to contouring and a more complex heat evacuation produced by the surrounding powder) [5,78]. This is in agreement with what it is observed in the microstructure of Fig. 12. Elongated primitive β grains are all oriented along the building direction. Specially for the case of more bulky samples (*e.g.*, 1.5 mm) where the heat flux is more unidirectional [78]. For the case of 0.5 mm, the granular β structure is more chaotic, although the preferred grain growth direction can still be inferred. This is the case due to a higher fraction of the area processed by the contouring strategy and the heat flux field present near to powder regions [78]. The prior-β grain boundaries are expected to have an effect on the mechanical behaviour of the material [79–81]. Zhang et al. [79], show the facility of the prior-β grain boundaries to

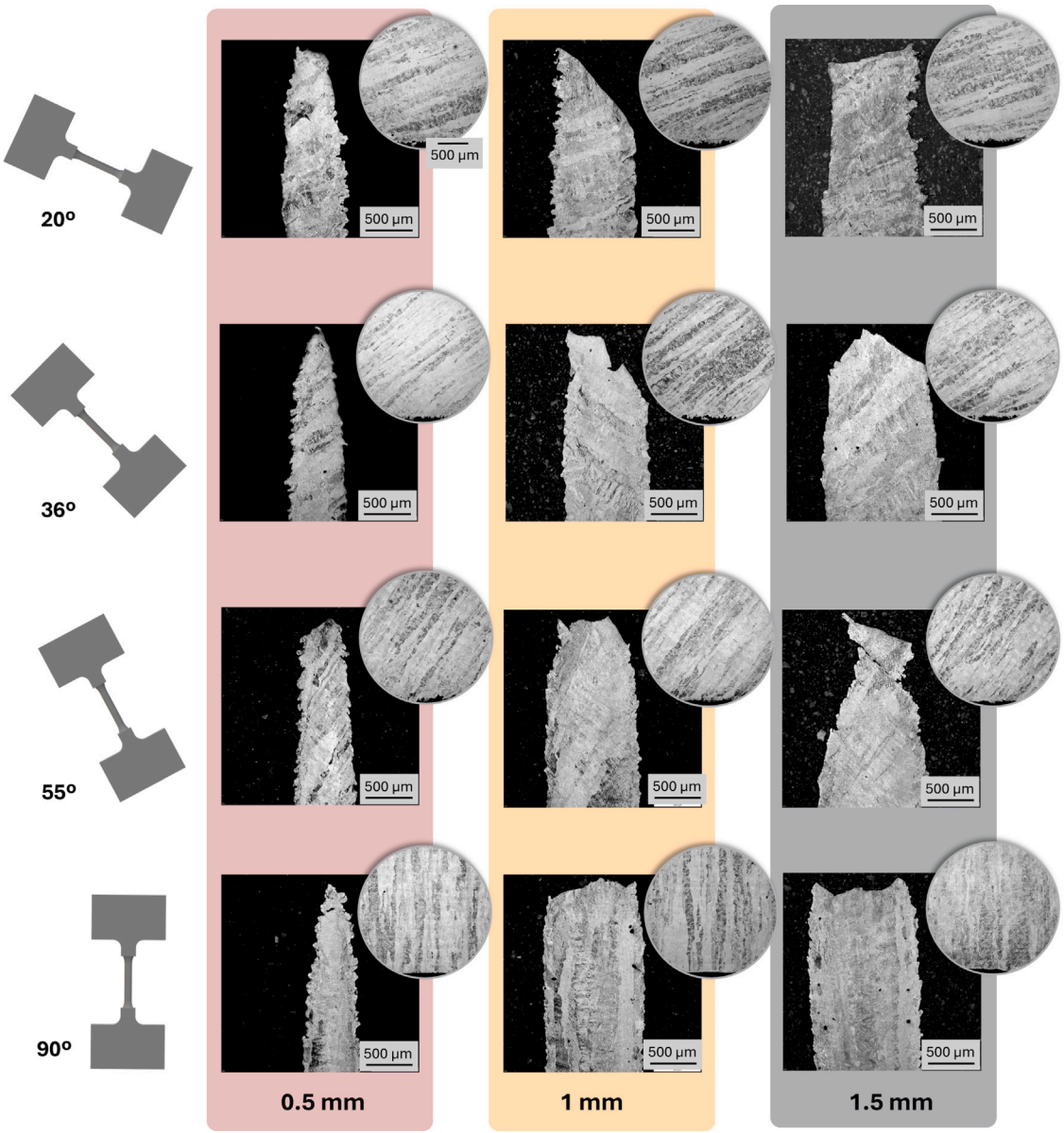

Fig. 12. Optical images of the microstructure observed for tested samples as function of the strut diameter and orientation. The scale marked in the first condition is the same for all orientation and diameter conditions.

act as nucleation sites for cracks in their work about laser directed energy deposition (LDED) Ti6Al4V. This can enhance the effect of higher surface defects observed for 20° in Fig. 10, which correspond also to the orientation with a higher fraction of prior-β grains oriented more perpendicularly to the load direction as seen in Fig. 12.

Fractography of elemental struts. The fractography images presented in Fig. 13 provide a detailed comparison of the fracture surfaces of representative tested struts for all the strut orientation and diameter conditions. By observation of the images, it is clear that the printing orientation has a marked effect on the eccentricity of the sample cross-section. For the case of vertical samples (90°), a perfect circular shape is observed for all the diameters. The shape of the cross-sectional surface become more elliptical as the strut get more tilted, specially for the smallest diameter. This is in agreement with previous studies in the literature [82] and it is associated with an overhang of accumulated molten material for low angle specimens.

In terms of the fracture surface, for all of the cases, there is presence of dimples associated with a ductile fracture. The size and shape of these dimples change in most cases from the centre of the fracture to the surface of the samples, where the size of the dimples decrease remarkably. This can be associated with the different stress conditions present in the centre of the sample and near to the surface [83] and also the higher temperature reached in the centre of the sample due to adiabatic heating [84].

For some cases, the fracture surfaces also present marks of smooth cleavage steps (*e.g.*, see Fig. 13-20° and 0.5 mm and 90° and 1.5 mm). These observations are consistent with previous studies in LDED Ti6Al4V [85] that observed that, while for quasi-static conditions quasi-cleavages and dimples were predominantly present, for the case of 1000 s^{-1} evenly distributed dimples between 2-10 µm with smooth step planes were observed. Furthermore, some marks associated with manufacturing voids and lack of fusion defects tipical from LPBF can be appreciated for some conditions (*e.g.*, see Fig. 13- 55°, 1 mm and 20°, 1.5 mm, respectively). Manufacturing voids are caused by gas trapped during the printing process and are usually round, while lack of fusion defects are characterized by its sharp edges [85], as seen in the centre of the 1.5 mm 55° strut. These defects can act as preferential sites for the nucleation of micro-cracks or stress concentration points [86].

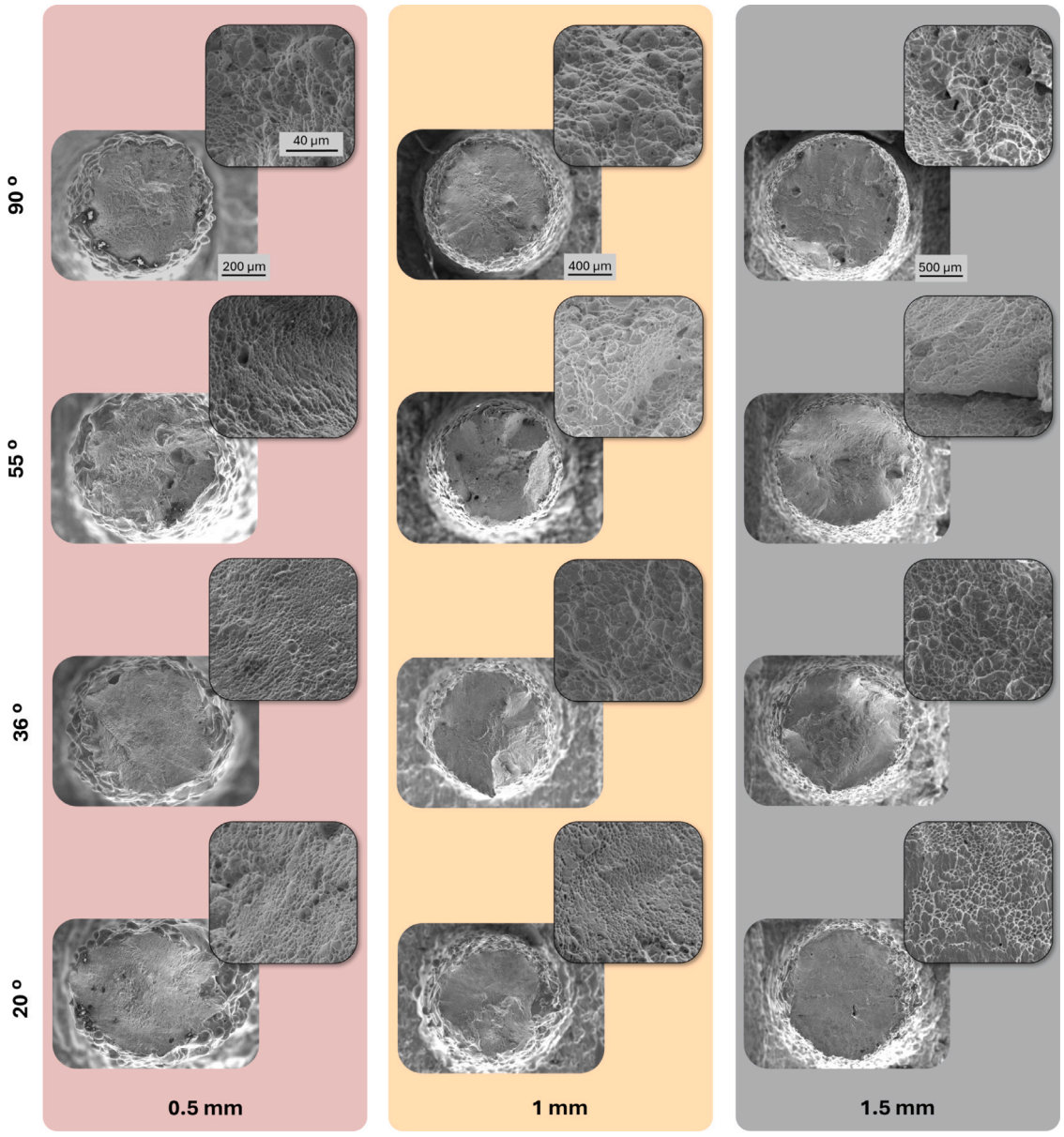

Fig. 13. Fracture surfaces of representative tested specimens for different strut diameter and orientation conditions. Along with them, detail of the centre region of each fracture surface is presented for dimple analysis.

For a deeper quantitative analysis, the size distribution of the dimples analysed at the centre of the samples is presented in Fig. 14. There is a visible trend indicating that the average size of the dimples increases for larger diameters and decreases as the struts are printed more tilted (*i.e.*, printing orientation decreases). This observation correlates with the curves observed in Fig. 8 and the analysis made in Section 3.1.2, where a more ductile behaviour was observed for the highest diameters and printing orientations. It can be observed that the increase in the dimple size is more pronounced between the 0.5 mm and 1 mm diameters, showing a certain stabilization when passing from 1 mm to 1.5 mm diameters except for the case of 20° (the most tilted struts), where the increment suggest a more linear trend. The orientation of the struts also influences the dimple size noticeably. At a 90° orientation, the average dimple size is at its peak, particularly for the 1.5 mm strut diameter, which measures approximately 8 µm. On the other hand, at a 20°, the average dimple size is the smallest, especially for the 0.5 mm diameter, which is approximately 2 µm. These values are in agreement with the dimples observed in the literature for AM Ti6Al4V tested under dynamic conditions [17,80].

3.2. Higher scale - Study of cellular structures

3.2.1. Relative density of the cellular structures and manufacturability

The measured relative density of each manufactured cellular structure condition is presented in Fig. 15 and compared with the ideal designed ones extracted from the CAD model. It can be observed that the standard deviation is negligible, which represent a good repeatability of the manufacturing process. As the diameter increases, there is a linear trend in which the relative density increases from ≈ 6% to ≈ 28.5%. Additionally, there is an excess of material for all cases when compared to the ideal designed solid fraction. This phenomenon has been previously seen in the literature [36,82,87] for similar lattice structures. The results in Fig. 15 show also a higher excess of material for vertical lattices when compared with the rotated counterparts. This can be rationalized by the orientation of the struts composing the lattice structures (see Fig. 2). For the case of vertically oriented lattices, all their struts are printed at an orientation of 36°, while for the case of the rotated lattices, 25% of their struts are oriented at 90° and 75% are oriented at 20°. As most of the struts in the rotated lattices are oriented

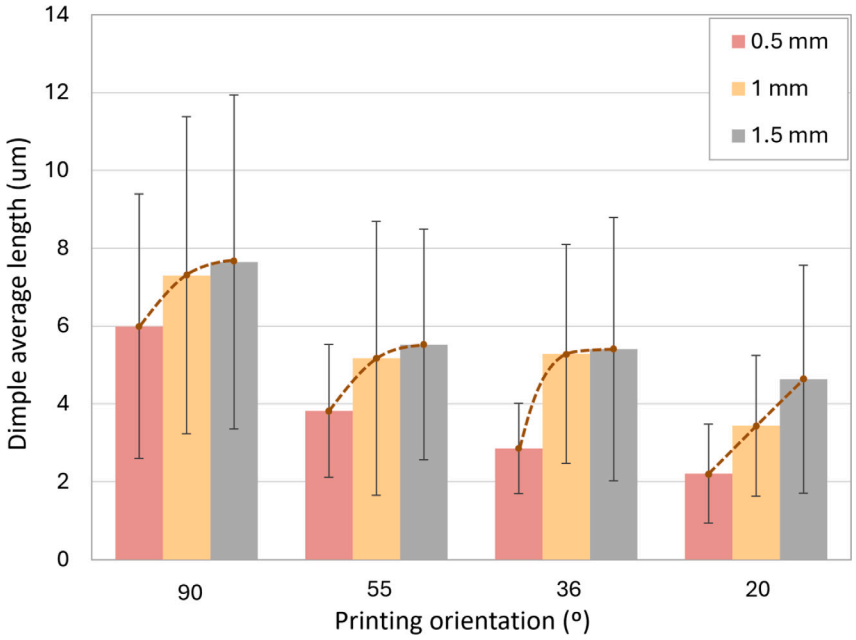

Fig. 14. Quantitative analysis of the dimple size in the centre of the struts corresponding to each condition (orientation and diameter), extracted from the images in Fig. 13.

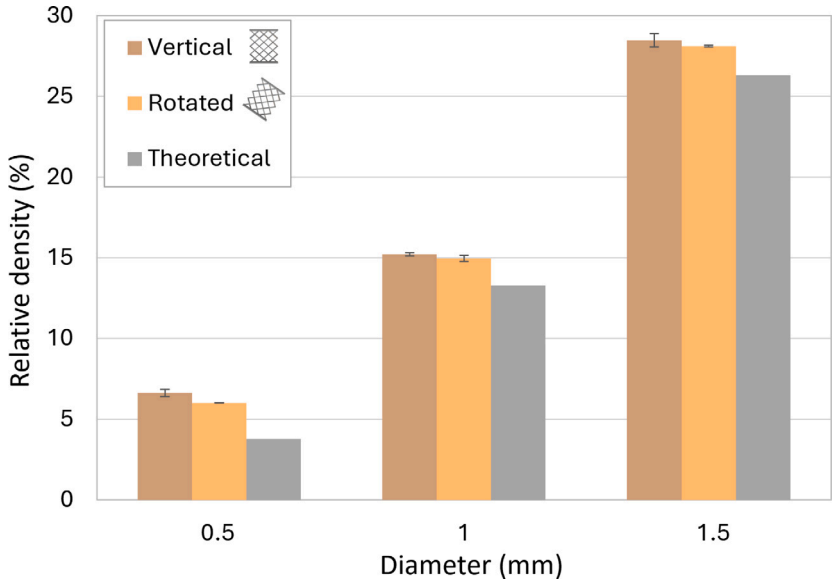

Fig. 15. Measured relative density of the BCC cellular structures compared with the ideal designed ones for the different lattice printing orientations and diameters under study.

at 20°, it is expected that these struts have a stronger influence in the material and the mechanical properties. As seen in Fig. 5, the struts oriented at 36° present a higher area than struts oriented at 20°, which is in agreement with the tendency observed for the measured relative fraction of the cellular structures.

3.2.2. *Mechanical behaviour of cellular structures*

Stress–strain dynamic curves. The mechanical response of the BCC cellular structures under compression obtained by direct impact Hopkinson pressure bar is presented in Fig. 16 in the form of engineering stress–strain curves. It is important to note that stress here refers to effective stress of the lattice, which is calculated as the total force exerted on the lattice divided by the total sample area (the squared cross sectional area of the sample). The strain refers to the effective strain as the total difference in displacement of the top and bottom plates divided by the height of the sample. A good reproducibility of the mechanical behaviour of the cellular structures can be observed, based on the low standard deviation values. The stress–strain characteristics exhibited by the lattices align with those observed in this type of lattices [88,89], indicating a response that is primarily influenced by bending-dominated mechanisms. In cellular structures and foams under compression, the initial elastic loading is followed by the initiation of plasticity, buckling or crushing, depending on the type of failure of the structure [90]. Following the theory proposed by Ashby et al. [90], after the onset of plasticity, collapse or crushing, the material continues to collapse at nearly constant stress up to densification or final failure. This is in agreement with the curves observed in Fig. 16. The specific particularities of the failure modes will be further discussed later.

By observing these curves, a weak effect of the lattice printing orientation on the mechanical behaviour can be inferred. On the other hand, there is a strong effect of the strut diameter (and relative density) on the mechanical behaviour. For all the cases, the stress plateau region

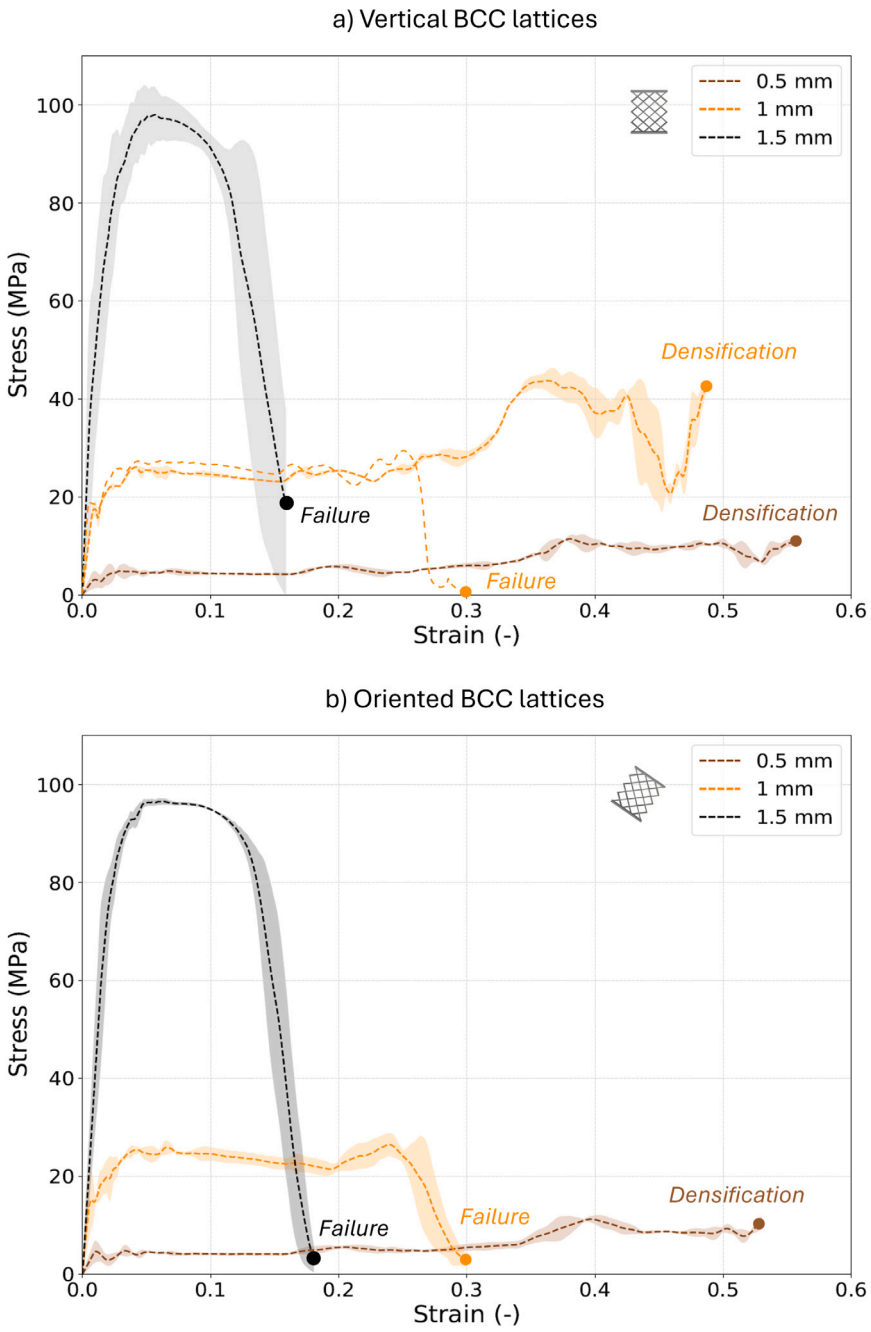

Fig. 16. Mechanical behaviour of the Ti6Al4V BCC structures as a function of strut diameter and lattice printing orientation. Shaded areas show the standard deviation, while the dashed lines indicate the averaged curves, derived from three repetitions per condition (same diameter and orientation). The nature of the end of the test is indicated: sudden failure for lattices which has failed abruptly (damage localization along a band of struts) or densification for lattices in which after initial failure of a range of struts, the load is transferred to the rest of the lattice, densifying.

seems to extend to larger strains when smaller diameters are used. The stress values of this plateau region increases with the strut diameter, as expected for BCC-type lattices [91]. This will be discussed next.

Plastic/crushing stress and plateau region. As stated before, the onset of plasticity or crushing is followed by a continuous collapse of the structure at nearly constant stress. This onset stress has been extracted from the stress–strain curves in Fig. 16 for each condition and it is shown in Fig. 17(a) as a function of the strut diameter. Typically, to reduce the complexity of the lattice design process, the driven design variable is the relative density [9,33,86,92], previously introduced. For this reason, the plastic/crushing stress has been also represented as function of the relative density in Fig. 17(b).

In terms of the effect of the strut thickness, the plastic/crushing stresses are consistent with the typical lattice behaviour observed in the literature, where increased strut thickness enhances the overall mechanical performance [91,92]. For example, Forés-Garriga et al. [92] studied the effect of the relative density of several polymeric lattice materials performing quasi-static tests and found a direct correlation between the relative density and mechanical properties such as elastic modulus, yield stress and UTS. In another study, Jin et al. [91] simulated four different LPBF Ti6Al4V lattice morphologies and analysed the effect of the relative density under dynamic loading (1000 s^{-1}). They found that compressive properties increased with relative density in all cases, following a power law with different coefficients corresponding to each architecture.

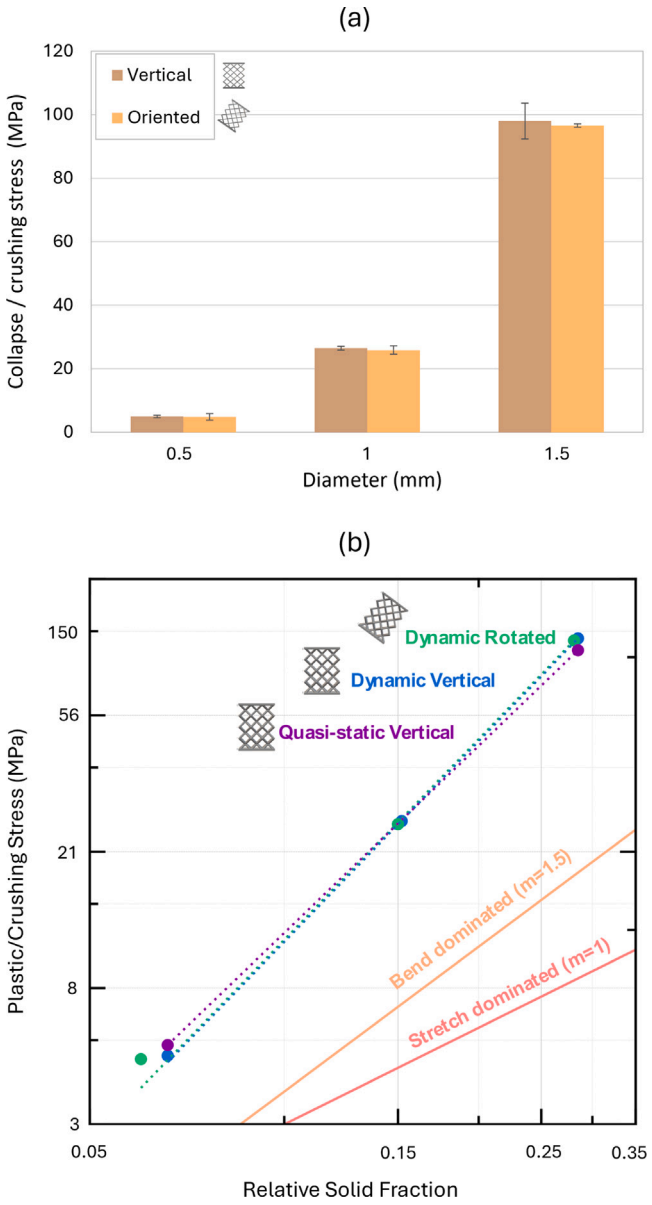

Fig. 17. (a) Plastic/crushing stress variation of BCC lattices with three different diameters printed vertically and oriented; (b) Ashby plot of UTS vs. solid fraction for the BCC lattices tested in this study. Literature points are indicated for Ref. [45].

In terms of the lattice printing orientation effect on the plastic/crushing stress is much less significant, as seen in Fig. 17(a). A slight increase in the onset stress is observed for the case of vertical lattices when compared to the rotated ones. This could be cause by the different strut mechancial behaviour observed at the lower scale in Figs. 9 and 11. For the case of the rotated lattice, the mechanical behaviour of the 20° struts is expected to dominate over the 90° due to its higher fraction (75% vs. 25%). The struts printed at 20° present similar mechanical behaviour to the ones printed at 36° (vertical lattice) in terms of peak flow stress for the case of 0.5 mm and 1.5 mm (higher scatter for the case of 0.5 mm). However, for the case of 1 mm, these 36° struts present a peak flow stress 6.3% higher than the 20° struts (rotated lattice). In any case, it is clear that the effect of strut diameter is stronger than strut orientation, proving the ability of using the relative density as an effective tuner for achieving the desired mechanical properties by changing the diameter of the struts, the architecture or the cell size.

Regarding the strain rate sensitivity of the peak flow stress, the values obtained in this study have been compared with the quasi-static properties of the previous work of Cardeña et al. [45]. The dynamic factors arising from the comparison are 1.13 for the case of the 0.5 mm diameter lattices and 1.10 for the case of 1.5 mm diameter lattices. These values are in agreement with previous studies of the literature [93]. Tancogne-Dejean and Dirk Mohr [93] reported a dynamic factor ranging from 1.17 to 1.31 for classical BCC and modified "tapered BCC" lattices made of 316L steel with relative densities similar to those in this study. The close agreement between these values and our findings, despite the different material used, underscores the significant influence of lattice architecture on the dynamic factor of these metamaterials.

Fig. 17(b) shows the relationship between the plastic/crushing stress and the relative density of the studied lattices as an "Ashby" plot [90]. Ashby et al. [90] established a power law relation between the plastic/crushing stress and the relative density of cellular structure in the form:

$$\frac{\sigma_c}{\sigma_y} \propto \left(\frac{\rho_c}{\rho_s}\right)^m \tag{8}$$

where σ_c is the onset of plasticity/crushing of the cellular structure, σ_y is the yield stress of the bulk material (Ti6Al4V), ρ_c is the density of the cellular material and ρ_s is the density of the bulk material (being $\frac{\rho_c}{\rho_s}$ the solid fraction). The exponent m is related to the loading mode of the lattice [90] and corresponds to the slope of the lines in Fig. 17. An exponent of $m = 1.0$ correspond to lattices in which their struts are dominated by stretching forces, while for the case of $m = 1.5$, the struts are predominantly under bending moments. By looking at the figure, one can observe that the slope for both dynamic and static conditions is closer to $m = 1.5$ which means that they have been working predominantly under bending dominated forces. This observation aligns well with predictions derived from earlier dynamic simulations involving Ti6Al4V lattices of BCC type [91] and other foundational studies for a wide range of lattice structures [87,90].

Energy absorption and ductility. Although the measurement of energy absorption (and ductility) before fracture is direct for bulk solid samples, a more complex methodology needs to be used for the case of cellular materials. As the material deforms, densification is reached when possible at a given strain, as can be observed in Fig. 16. The concept of densification can be described as the point after the plateau region in which the opposite sides of the cells are forced into contact and further deformation is not possible [90]. There are different approaches to address the energy absorption properties of the cellular materials [42,91,94]. The approach followed in this study is the one from Harris et al. [42], based on two metrics that determine the energy absorption performance of lattice metamaterials from an impact mitigation perspective: the capacity to absorb energy before densification (energy absorption capacity) and the peak stresses during the deformation process until densification (energy absorption efficiency).

For the first metric, in the assumption of uniform deformation, the area below the stress–strain curve is computed as the volumetric energy absorption W of the lattice up to the densification strain ε_d (obtained by the method used in the second metric):

$$W(\varepsilon_d) = \int_0^{\varepsilon_d} \sigma \, d\varepsilon \tag{9}$$

For the sake of comparison between different relative densities, the mass normalized version of the energy absorbed $\overline{W}(\varepsilon_d)$ can be computed as:

$$\overline{W}(\varepsilon_d) = \frac{1}{\rho_r \rho_s} \int_0^{\varepsilon_d} \sigma \, d\varepsilon \tag{10}$$

where ρ_r denotes the lattice relative density and ρ_s refers to the density of the bulk material.

The second metric is based on the energy absorption efficiency method introduced by Tan et al. [95] in their work about aluminium

foams, later adapted to cellular materials by Harris et al. [42]. The energy absorption efficiency η is used to compute the densification strain and analyse the overall peformance:

$$\eta(\varepsilon_1) = \frac{1}{\sigma_m(\varepsilon_1)} \int_0^{\varepsilon_1} \sigma \, d\varepsilon \tag{11}$$

This metric considers the relation between the cumulative volumetric energy absorption capacity W to the maximum stress σ_m experienced up to a given strain value ε_1. The densification strain ε_d is defined as the strain which maximizes the energy absorption efficiency η (Eq. (11)). As observed, this method defined unambiguously the densification point of the curve.

Based on this methodology, the volumetric energy absorption $W(\varepsilon_d)$, its normalized counterpart $\overline{W}(\varepsilon_d)$ and the maximum value of the energy absorption efficiency η are presented in Fig. 18. The values presented here for $W(\varepsilon_d)$ are in accordance with previous studies in the literature [45,91,96]. Zhao et al. [96] found similar values of absorbed energy up to 50% deformation when studying simple and TPMS LPBF Ti6Al4V BCC lattices during quasi-static compression tests with similar volume fractions (10%, 20% and 30%). The values for the energy absorbed in their study at 50% strain were almost identical to the results shown in Fig. 18 for lower strains, which is also consistent with the results from Cardeña et al. [45], indicating that the energy absorption is higher for the same lattice architecture when exposed to dynamic regimes. In comparison to other dynamic investigations, Jin et al. [91] study the energy absorption capabilities of various Ti6Al4V lattice structures up to a 20% strain through numerical simulations, showing results with a high level of agreement compared to the ones illustrated in Fig. 18.

A critical aspect to consider affecting the energy absorption is the loading nature of the lattice, *i.e.*, stretch dominated or bend dominated. While stretch dominated structures show high elastic modulus and yield strength, bending dominated structures present exceptional energy absorption properties [35]. As stated before in Fig. 17(b), the BCC present a bending dominated behaviour. This is the reason behind the study of BCC structures for energy absorption and impact applications in the literature [91,93,97,98].

In terms of the effect of the strut diameter in Fig. 18(a), larger diameters contribute to greater load-bearing capacity and energy absorption $W(\varepsilon_d)$, as seen specially for the case of 1.5 mm diameter by the wider area below the curve and higher stress values observed in Fig. 16. This trend vanishes when normalizing the energy by the relative density as observed in Fig. 18(b). The energy absorbed per unit mass $\overline{W}(\varepsilon_d)$ is much closer for the three diameters, presenting an opposite trend in which the energy absorbed per unit mass is slightly higher for the case of the smallest diameter, being the energy of the 1 mm diameter and 1.5 mm diameter very similar. The trend observed in our study appears to contradict the expected behaviour as described in the numerical findings presented in [91]. Based on these results, it is expected that a positive correlation exists between the energy absorbed per unit mass and the relative density of the lattice structure. This implies that as the relative density increases, the amount of energy that can be absorbed per unit mass also increases. However, there are two critical considerations that may shed light on these discrepancies. Firstly, in [91], the energy absorbed was calculated only up to 20% strain. Secondly, while the collapse behaviour in the simulations remains consistent, the experiments reveal a notable dependency on the strut diameter. Variations in diameter lead to distinct failure modes of the lattice. This point will be explored in more detail in the following section.

When considering the orientation dependence in Fig. 18(a)–(b), it can be observed that the energy absorbed by the vertical lattices is very similar to the energy absorbed by the rotated ones (despite for the case of 1 mm), suggesting that printing orientation has a minor role in this feature. For the case of 1 mm diameter, the differentiation between vertical and oriented values is caused by the presence of two well differentiated failure modes that will be explain in the following section.

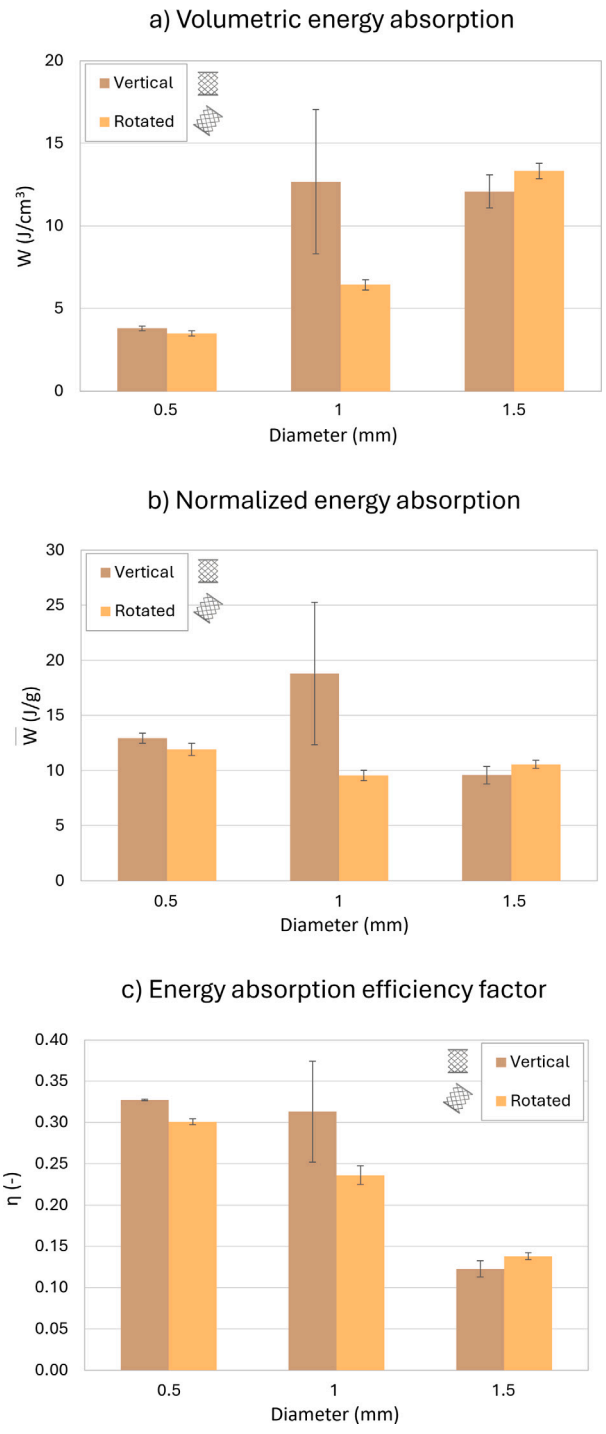

Fig. 18. (a) Volumetric energy absorption $W(\varepsilon_d)$, corresponding to each condition (diameter and orientation); Normalized energy absorption $\overline{W}(\varepsilon_d)$, corresponding to each condition (diameter and orientation); (c) Maximum value of the energy absorption efficiency factor η of the BCC lattices, corresponding to each condition (diameter and orientation).

In Fig. 18(c), the energy absorption efficiency η is presented for every diameter and orientation. In this case, the trend is the opposite as for the energy absorbed $W(\varepsilon_d)$, since higher diameters present a lower energy absorption efficiency. The efficiency is lower for bigger diameters since the maximum stress reached (which is the divisor in Eq. (11)) is exponentially higher while the energy absorbed remains much more similar between the diameters. This suggests that lattices

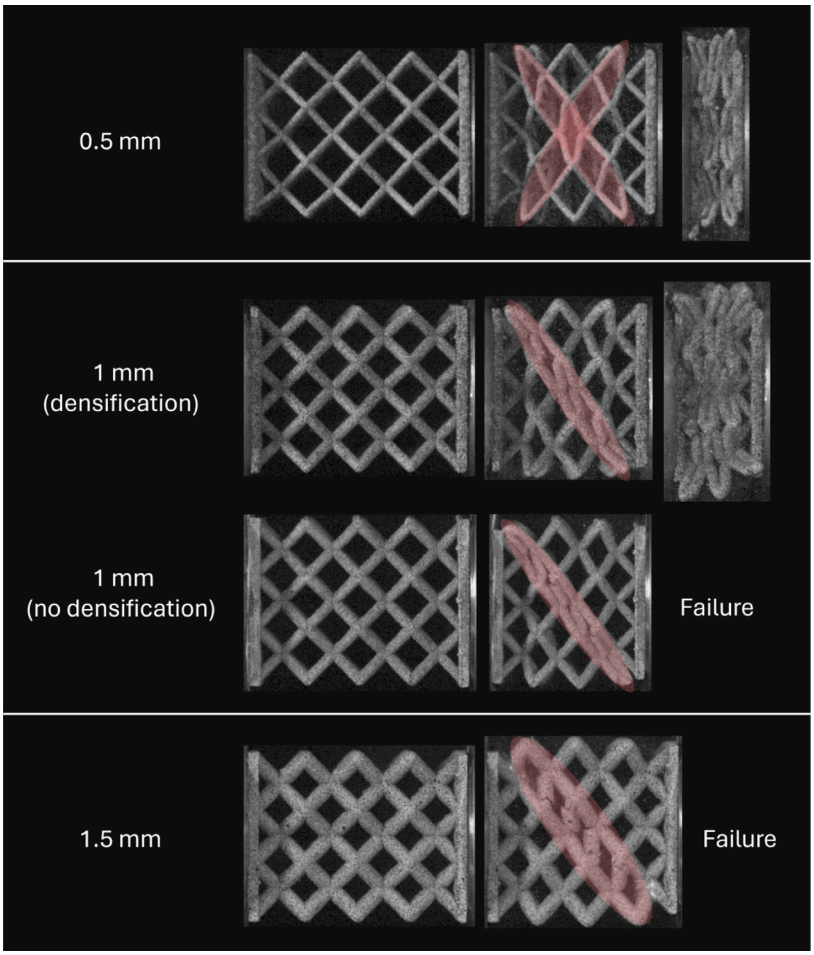

Fig. 19. Failure modes of the BCC lattices depending on the diameter. The general failure modes are shown, as they are identical in vertical and rotated lattices. The only exception is the 1 mm diameter case, where two different failure modes are observed for the case of the vertical lattices.

with lower relative densities are more efficient at absorbing higher values of impact energy while subjecting the structure to lower stress levels.

Failure modes. At this stage, it is clear that energy absorption and failure modes are closely related. Different collapse modes can result in higher strains to failure, allowing the material to continue absorbing energy as it deforms further. Moreover, the different shapes of the curves from Fig. 16 suggest different collapsing modes depending on the strut diameter. To further analyse the failure mode, the representative deformation events preceding the failure for each strut diameter condition are presented in Fig. 19.

For the case of 0.5 mm strut diameter, all the lattices reached densification at strain values of approximately 55%, as indicated by the increase of the bearing load. Conversely, for the case of the 1.5 diameter, a different process occurs involving a sudden fracture after the plateau at about 18% strain, with the stress dropping to zero.

No difference was found for vertical and rotated lattices for the case of 0.5 mm and 1.5 mm. For 1 mm diameter, vertical samples present more than one failure mode: some of the samples reached densification like the 0.5 mm lattices, leading to a higher stress value before failing, and the others present the sudden fracture behaviour observed in the 1.5 mm lattices. The densification was observed for 2/3 of the vertical samples while in the rotated batch, all of them failed without densifying. This behaviour suggests that the 1 mm diameter vertical lattices represent a transition area in which the collapsing mode of the BCC goes from densification to classical failure at 45° as the diameter increases.

It is expected that the mechanical behaviour of the elemental struts observed in Section 3.1 triggers this transition. The presence of struts with lower load bearing capability can lead to a controlled failure of the structure (much less energetic) that can be transferred to the rest of the lattice, allowing the densification, as observed in Fig. 19. However, for the case of thicker struts, the high elastic energy stored in each of the struts is suddenly liberated after the first fracture, which can lead to the formation of localized shear bands and sudden collapse, preventing the densification of the lattice.

As seen in the figure, all the samples have deformation localization at the beginning of the damage with the formation of a shearband at 45° that goes from one side of the lattice to the other. The diagonal shearband is formed by the buckling of the individual struts, according to the bending-dominated nature of this architecture [87]. For the case of the 0.5 mm diameter lattices, two symmetric shearbands are observed with the same 45° angle. The deformation is homogeneous and the sample keeps deforming until densification. No localized failures are observed until the final stage, being the nodes the areas of breakage at that point. Regarding the 1.5 mm diameter lattices, all of them broke after the formation of the shearband, reaching significant lower values of maximum strains compared to the 0.5 mm and 1 mm diameters. Specifically, the failure also occurred in the nodes of the localized band. Mines et al. [98] studied the collapsing behaviour of LPBF Ti6Al4V BCC microlattices and found prevalence of local failure at individual nodes promoting the formation of the diagonal bands. They also associated the appearance of symmetric bands with more ductility. This is consistent with the results observed in Fig. 16.

By observing this study, it is clear that the mechanical behaviour of the underlying elementals can control the macroscopic behaviour of the lattice structure. The collapsing mode studied in this section brings out the importance of analysing the loading state of the elements of the lattice to be able to tune the stress distribution and make the most out of the single struts properties.

4. Conclusions

In this work, the effect of the printing geometry and the orientation on the mechanical performance of cellular materials (*i.e.*, BCC) has been addressed. To do so, two different scales have been studied: (1) the intrinsic material properties of the foundational elemental struts manufactured at 20°, 36°, 55° and 90° orientations and 0.5 mm, 1 mm and 1.5 mm diameters; (2) the macroscopic mechanical properties of the cellular structure manufactured vertically and rotated (45° along X axis and 35° along Y axis) with 0.5 mm, 1 mm and 1.5 mm diameters. Based on the observed results, the following conclusions can be drawn:

1. Regarding the precision of the strut manufacturing and their microstructure:
    - Geometrical accuracy: As the strut diameter decreases, the deviation from the ideal designed diameter increases drastically, reaching up 70%–90% for 0.5 mm. The effect of printing orientation is minor, with a slight decrease of the printing accuracy as the struts are printed more vertically.
    - Surface roughness: The average roughness of the downskin is higher than the upper skin for all orientation and diameters. The difference between upperskin and downskin roughness is more pronounced as the struts are more tilted. No significant effect of the strut thickness was found in the roughness values.
    - Microstructure: Elongated primitive β grains are all oriented along the building direction. Specially for the case of more bulky samples (*e.g.*, 1.5 mm) where the heat flux is more unidirectional.
2. Regarding the dynamic mechanical performance of the struts:
    - Different stress–strain curve shapes were observed for 0.5 mm (bell shaped) when compared to 1 and 1.5 mm struts (peak, followed by plateau and then fracture). This has been rationalized by the different effects of the thermal softening on the three strut diameters.
    - Strain to failure: Higher values of strain to failure were measured for dynamic conditions when compared to static conditions in the literature. This has been rationalized by the thermal softening produced by the sudden plastic deformation. A larger strut diameter results in a significant increase of the strain to failure. This has been connected to the higher effect of the thermal softening for larger samples and the higher impact of stress concentrators and defects for smaller samples. Finally, in terms of orientation, 20° struts present the lower strain to failure regardless of the strut diameter, with 36, 55 and 90° presenting similar ductility among them. A direct correlation has been found between the strain to failure and the size of the dimples of the fracture surface.
    - Peak flow stress: The peak flow stresses for all the conditions are enclosed in the range of $\approx$ 1850 and 2200 MPa. 1.5 mm struts present lower average peak flow stress for most orientations, except for 55°. Conversely, 1 mm diameter struts present the higher peak flow stresses for all orientations. These trends have been rationalized by the competing effects of microstructure refinement for smaller struts and the higher effect of critical defects as strut size decreases. No clear trend was observed for the case of the orientation.
3. Regarding the accuracy of the cellular material manufacturing:
    - Relative density: There is an excess of material for all cases when compared to the ideal designed relative density. The results show also a higher excess of material for vertical lattices when compared with the rotated counterparts. This has been rationalized by the orientation of the struts composing the lattice structures.
4. Regarding the dynamic mechanical performance of cellular materials:
    - The stress–strain curves exhibited by the lattices align with those primarily influenced by bending-dominated mechanisms. The initial elastic loading is followed by the initiation of plasticity/crushing and then the material continues to collapse at nearly constant stress up to densification or final failure.
    - Plastic/Crushing Stress: In terms of the effect of the strut thickness, the plastic/crushing stress increases for larger strut diameters. The ‘‘Ashby’’ coefficient for these lattices under dynamic conditions is close to bend-dominated mode (m = 1.5). The effect of the lattice printing orientation on the plastic/crushing stress is much less significant than the strut diameter effect.
    - Energy absorption: An analysis based on the volumetric energy absorption $W(\varepsilon_d)$ and the energy absorption efficiency η has been done. The results shows that larger strut diameters result into larger energy absorption values. This trend vanishes when normalizing the energy by the relative density. The printing orientation has a minor role in the volumetric absorbed energy. For the case of η, the trend is opposite, since higher diameters present a lower energy absorption efficiency.
    - Failure modes: A distinct failure mode has been observed as a function of the strut diameter. 0.5 mm lattices present densification, while 1.5 mm lattices present an abrupt fracture with the formation of a 45° shear band. For the case of 1 mm lattices, a mix between densification and abrupt fracture has been observed, suggesting that this is a transition diameter in the collapsing mode of the lattice.

CRediT authorship contribution statement

Andrea Cardeña: Writing – review & editing, Writing – original draft, Methodology, Investigation, Data curation, Conceptualization. **Rafael Sancho:** Writing – review & editing, Writing – original draft, Supervision, Methodology, Investigation, Conceptualization. **Francisco Gálvez:** Writing – review & editing, Supervision, Methodology, Investigation, Conceptualization. **Sergio Perosanz:** Writing – review & editing, Methodology, Investigation. **Daniel Barba:** Writing – review & editing, Writing – original draft, Supervision, Methodology, Investigation, Funding acquisition, Conceptualization.

Declaration of competing interest

The authors declare that they have no known competing financial interests or personal relationships that could have appeared to influence the work reported in this paper.

Acknowledgements

Grant PID2020-116440RA-I00 funded by MICIU/AEI/10.13039/501100011033.

Grant PRE2021-097388 funded by MICIU/AEI/10.13039/501100011033 and by ESF+.

Grant EQC2019-006491-P funded by MICIU/AEI/10.13039/501100011033 and by ERDF A way of making Europe.

Appendix A. Supplementary data

Supplementary material related to this article can be found online at https://doi.org/10.1016/j.ijimpeng.2025.105294.

Data availability

Data will be made available on request.

References

[1] Veiga C, Davim JP, Loureiro A. Properties and applications of titanium alloys: A brief review. Rev Adv Mater Sci 2012;32:133–48.
[2] Inagaki I, Takechi T, Ariyasu YSN. Application and features of titanium for the aerospace industry. 2014, URL https://api.semanticscholar.org/CorpusID:138460261.
[3] Salehi S-D, Beal R, Kingstedt OT. Dynamic behavior and thermomechanical characterization of laser powder bed fusion and wrought Ti–6Al–4V. Int J Impact Eng 2023;176:104552. http://dx.doi.org/10.1016/j.ijimpeng.2023.104552, URL https://www.sciencedirect.com/science/article/pii/S0734743X23000635.
[4] Vilella T, Rodríguez D, Fargas G. Additive manufacturing of Ni-free Ti-based shape memory alloys: A review. Biomater Adv 2024;158:213774. http://dx.doi.org/10.1016/j.bioadv.2024.213774, URL https://www.sciencedirect.com/science/article/pii/S2772950824000177.
[5] Barba D, Alabort C, Tang Y, Viscasillas M, Reed R, Alabort E. On the size and orientation effect in additive manufactured Ti-6Al-4V. Mater Des 2020;186:108235. http://dx.doi.org/10.1016/j.matdes.2019.108235, URL https://www.sciencedirect.com/science/article/pii/S0264127519306732.
[6] Simonelli M, Tse Y, Tuck C. Effect of the build orientation on the mechanical properties and fracture modes of SLM Ti–6Al–4V. Mater Sci Eng: A 2014;616:1–11. http://dx.doi.org/10.1016/j.msea.2014.07.086, URL https://www.sciencedirect.com/science/article/pii/S0921509314009538.
[7] Krakhmalev P, Fredriksson G, Yadroitsava I, Kazantseva N, du Plessis A, Yadroitsev I. Deformation behavior and microstructure of Ti6Al4V manufactured by SLM. Phys Procedia 2016;83:778–88. http://dx.doi.org/10.1016/j.phpro.2016.08.080, Laser Assisted Net Shape Engineering 9 International Conference on Photonic Technologies Proceedings of the LANE 2016 September 19–22, 2016 Fürth, Germany, URL https://www.sciencedirect.com/science/article/pii/S1875389216301870.
[8] Aghajani S, Wu C, Li Q, Fang J. Additively manufactured composite lattices: A state-of-the-art review on fabrications, architectures, constituent materials, mechanical properties, and future directions. Thin-Walled Struct 2024;197:111539. http://dx.doi.org/10.1016/j.tws.2023.111539, URL https://www.sciencedirect.com/science/article/pii/S0263823123010169.
[9] Liu S, Shin YC. Additive manufacturing of Ti6Al4V alloy: A review. Mater Des 2019;164:107552. http://dx.doi.org/10.1016/j.matdes.2018.107552, URL https://www.sciencedirect.com/science/article/pii/S026412751830916X.
[10] Liu Y, Wang T, Chen H, Li Z, Li S, Wang D, et al. Impact behaviors of additively manufactured metals and structures: A review. Int J Impact Eng 2024;191:104992. http://dx.doi.org/10.1016/j.ijimpeng.2024.104992, URL https://www.sciencedirect.com/science/article/pii/S0734743X24001167.
[11] McKenna T, Tomonto C, Duggan G, Lalor E, O'Shaughnessy S, Trimble D. Evaluation of bimodal microstructures in selective-laser-melted and heat-treated Ti-6Al-4V. Mater Des 2023;227:111700. http://dx.doi.org/10.1016/j.matdes.2023.111700, URL https://www.sciencedirect.com/science/article/pii/S0264127523001156.
[12] June D, Mayeur JR, Gradl P, Wessman A, Hazeli K. Effects of size, geometry, and testing temperature on additively manufactured Ti-6Al-4V titanium alloy. Addit Manuf 2024;80:103970. http://dx.doi.org/10.1016/j.addma.2024.103970, URL https://www.sciencedirect.com/science/article/pii/S2214860424000162.
[13] Casata M, Perosanz S, Garrido C, Barba D. A holistic study of the effect of geometrical and processing conditions on the static mechanical performance of LPBF strut elements. Mater Des 2024;247:113387. http://dx.doi.org/10.1016/j.matdes.2024.113387, URL https://www.sciencedirect.com/science/article/pii/S0264127524007627.
[14] Singla AK, Banerjee M, Sharma A, Singh J, Bansal A, Gupta MK, et al. Selective laser melting of Ti6Al4V alloy: Process parameters, defects and post-treatments. J Manuf Process 2021;64:161–87. http://dx.doi.org/10.1016/j.jmapro.2021.01.009, URL https://www.sciencedirect.com/science/article/pii/S1526612521000281.
[15] Gong H, Rafi K, Gu H, Janaki Ram G, Starr T, Stucker B. Influence of defects on mechanical properties of Ti–6Al–4V components produced by selective laser melting and electron beam melting. Mater Des 2015;86:545–54. http://dx.doi.org/10.1016/j.matdes.2015.07.147, URL https://www.sciencedirect.com/science/article/pii/S0264127515302161.
[16] Thijs L, Verhaeghe F, Craeghs T, Humbeeck JV, Kruth J-P. A study of the microstructural evolution during selective laser melting of Ti–6Al–4V. Acta Mater 2010;58(9):3303–12. http://dx.doi.org/10.1016/j.actamat.2010.02.004, URL https://www.sciencedirect.com/science/article/pii/S135964541000090X.
[17] Yuan Y, Zhang Y, Qiao Y, Xie J, Xu Q, Qi Y, et al. Effect of build orientation on dynamic compressive behaviour of Ti-6Al-4V alloy fabricated by selective laser melting. Mater Sci Eng: A 2023;862:144440. http://dx.doi.org/10.1016/j.msea.2022.144440, URL https://www.sciencedirect.com/science/article/pii/S0921509322018202.
[18] Liu Y, Meng J, Zhu L, Chen H, Li Z, Li S, et al. Dynamic compressive properties and underlying failure mechanisms of selective laser melted Ti-6Al-4V alloy under high temperature and strain rate conditions. Addit Manuf 2022;54:102772. http://dx.doi.org/10.1016/j.addma.2022.102772, URL https://www.sciencedirect.com/science/article/pii/S2214860422001762.
[19] Yang L, Zhicong P, Ming L, Yonggang W, Di W, Changhui S, et al. Investigation into the dynamic mechanical properties of selective laser melted Ti-6Al-4V alloy at high strain rate tensile loading. Mater Sci Eng: A 2019;745:440–9. http://dx.doi.org/10.1016/j.msea.2019.01.010, URL https://www.sciencedirect.com/science/article/pii/S0921509319300097.
[20] Alkhatib SE, Sercombe TB. High strain-rate response of additively manufactured light metal alloys. Mater Des 2022;217:110664. http://dx.doi.org/10.1016/j.matdes.2022.110664, URL https://www.sciencedirect.com/science/article/pii/S0264127522002854.
[21] Zhicong P, Yang L, Ming L, Chunli Z, Shuxin L, Yonggang W, et al. Influence of process parameter and strain rate on the dynamic compressive properties of selective laser-melted Ti-6Al-4V alloy. Appl Phys A 2019;125(2). http://dx.doi.org/10.1007/s00339-018-2359-x.
[22] Cui Y, Cai J, Li Z, Jiao Z, Hu L, Hu J. Effect of porosity on dynamic response of additive manufacturing Ti-6Al-4V alloys. Micromachines 2022;13(3). http://dx.doi.org/10.3390/mi13030408, URL https://www.mdpi.com/2072-666X/13/3/408.
[23] Zhang X, Zhou H, Shi W, Zeng F, Zeng H, Chen G. Vibration tests of 3D printed satellite structure made of lattice sandwich panels. AIAA J 2018;56(10):4213–7. http://dx.doi.org/10.2514/1.J057241.
[24] Bühring J, Nuño M, Schröder K-U. Additive manufactured sandwich structures: Mechanical characterization and usage potential in small aircraft. Aerosp Sci Technol 2021;111:106548. http://dx.doi.org/10.1016/j.ast.2021.106548, URL https://www.sciencedirect.com/science/article/pii/S1270963821000596.
[25] Ferro CG, Varetti S, Maggiore P. Experimental evaluation of mechanical compression of lattice trusses made with Ti6Al4V for aerospace use. Chin J Aeronaut 2024;37(5):520–32. http://dx.doi.org/10.1016/j.cja.2024.02.005, URL https://www.sciencedirect.com/science/article/pii/S1000936124000499.
[26] Ferro CG, Varetti S, De Pasquale G, Maggiore P. Lattice structured impact absorber with embedded anti-icing system for aircraft wings fabricated with additive SLM process. Mater Today Commun 2018;15:185–9. http://dx.doi.org/10.1016/j.mtcomm.2018.03.007, URL https://www.sciencedirect.com/science/article/pii/S235249281730154X.
[27] Fuganti A, Lorenzi L, Grønsund A, Langseth M. Aluminum foam for automotive applications. Adv Eng Mater 2000;2(4):200–4. http://dx.doi.org/10.1002/(SICI)1527-2648(200004)2:4<200::AID-ADEM200>3.0.CO;2-2, URL https://onlinelibrary.wiley.com/doi/abs/10.1002/%28SICI%291527-2648%28200004%292%3A4%3C200%3A%3AAID-ADEM200%3E3.0.CO%3B2-2.
[28] du Plessis A, Broeckhoven C, Yadroitsava I, Yadroitsev I, Hands CH, Kunju R, et al. Beautiful and functional: A review of biomimetic design in additive manufacturing. Addit Manuf 2019;27:408–27. http://dx.doi.org/10.1016/j.addma.2019.03.033, URL https://www.sciencedirect.com/science/article/pii/S2214860419302611.

[29] Ozdemir Z, Hernandez-Nava E, Tyas A, Warren JA, Fay SD, Goodall R, et al. Energy absorption in lattice structures in dynamics: Experiments. Int J Impact Eng 2016;89:49–61. http://dx.doi.org/10.1016/j.ijimpeng.2015.10.007, URL https://www.sciencedirect.com/science/article/pii/S0734743X15002134.

[30] Tyagi SA, M. M. Additive manufacturing of titanium-based lattice structures for medical applications – A review. Bioprinting 2023;30:e00267. http://dx.doi.org/10.1016/j.bprint.2023.e00267, URL https://www.sciencedirect.com/science/article/pii/S2405886623000106.

[31] Borikar GP, Patil AR, Kolekar SB. Additively manufactured lattice structures and materials: Present progress and future scope. Int J Precis Eng Manuf 2023;30. http://dx.doi.org/10.1007/s12541-023-00848-x.

[32] Pei E, Kabir I, Breški T, Godec D, Nordin A. A review of geometric dimensioning and tolerancing (GD&T) of additive manufacturing and powder bed fusion lattices. Prog Addit Manuf 2022;7. http://dx.doi.org/10.1007/s40964-022-00304-8.

[33] Simoes M, Harris J, Ghouse S, Hooper P, McShane G. Process parameter sensitivity of the energy absorbing properties of additively manufactured metallic cellular materials. Mater Des 2022;224:111398. http://dx.doi.org/10.1016/j.matdes.2022.111398, URL https://www.sciencedirect.com/science/article/pii/S0264127522010218.

[34] Noronha J, Rogers J, Leary M, Kyriakou E, Inverarity S, Das R, et al. Ti-6Al-4V hollow-strut lattice materials by laser powder bed fusion. Addit Manuf 2023;72:103637. http://dx.doi.org/10.1016/j.addma.2023.103637, URL https://www.sciencedirect.com/science/article/pii/S2214860423002506.

[35] Zhao M, Zhang DZ, Li Z, Zhang T, Zhou H, Ren Z. Design, mechanical properties, and optimization of BCC lattice structures with taper struts. Compos Struct 2022;295:115830. http://dx.doi.org/10.1016/j.compstruct.2022.115830, URL https://www.sciencedirect.com/science/article/pii/S0263822322006006.

[36] Liu L, Kamm P, García-Moreno F, Banhart J, Pasini D. Elastic and failure response of imperfect three-dimensional metallic lattices: the role of geometric defects induced by Selective Laser Melting. J Mech Phys Solids 2017;107:160–84. http://dx.doi.org/10.1016/j.jmps.2017.07.003, URL https://www.sciencedirect.com/science/article/pii/S0022509616307608.

[37] Sokollu B, Gulcan O, Konukseven EI. Mechanical properties comparison of strut-based and triply periodic minimal surface lattice structures produced by electron beam melting. Addit Manuf 2022;60:103199. http://dx.doi.org/10.1016/j.addma.2022.103199, URL https://www.sciencedirect.com/science/article/pii/S2214860422005887.

[38] Wauthle R, Vrancken B, Beynaerts B, Jorissen K, Schrooten J, Kruth J-P, Van Humbeeck J. Effects of build orientation and heat treatment on the microstructure and mechanical properties of selective laser melted Ti6Al4V lattice structures. Addit Manuf 2015;5:77–84. http://dx.doi.org/10.1016/j.addma.2014.12.008, URL https://www.sciencedirect.com/science/article/pii/S2214860414000323.

[39] Choy SY, Sun C-N, Leong KF, Wei J. Compressive properties of Ti-6Al-4V lattice structures fabricated by selective laser melting: Design, orientation and density. Addit Manuf 2017;16:213–24. http://dx.doi.org/10.1016/j.addma.2017.06.012, URL https://www.sciencedirect.com/science/article/pii/S221486041730026X.

[40] Smith M, Cantwell W, Guan Z, Tsopanos S, Theobald M, Nurick G, et al. The quasi-static and blast response of steel lattice structures. J Sandw Struct Mater 2011;13(4):479–501. http://dx.doi.org/10.1177/1099636210388983.

[41] Harris J, McShane G. Impact response of metallic stacked origami cellular materials. Int J Impact Eng 2021;147:103730. http://dx.doi.org/10.1016/j.ijimpeng.2020.103730, URL https://www.sciencedirect.com/science/article/pii/S0734743X20308009.

[42] Harris J, Winter R, McShane G. Impact response of additively manufactured metallic hybrid lattice materials. Int J Impact Eng 2017;104:177–91. http://dx.doi.org/10.1016/j.ijimpeng.2017.02.007, URL https://www.sciencedirect.com/science/article/pii/S0734743X16306947.

[43] Calladine C, English R. Strain-rate and inertia effects in the collapse of two types of energy-absorbing structure. Int J Mech Sci 1984;26(11):689–701. http://dx.doi.org/10.1016/0020-7403(84)90021-3, URL https://www.sciencedirect.com/science/article/pii/0020740384900213.

[44] Gangireddy S, Komarasamy M, Faierson EJ, Mishra RS. High strain rate mechanical behavior of Ti-6Al-4V octet lattice structures additively manufactured by selective laser melting (SLM). Mater Sci Eng: A 2019;745:231–9. http://dx.doi.org/10.1016/j.msea.2018.12.101, URL https://www.sciencedirect.com/science/article/pii/S0921509318318021.

[45] Cardeña A, Sancho R, Barba D, Gálvez F. Dynamic behaviour of additively manufactured Ti6Al4V BCC lattice-based structures. Mater Lett 2024;354:135286. http://dx.doi.org/10.1016/j.matlet.2023.135286, URL https://www.sciencedirect.com/science/article/pii/S0167577X23014714.

[46] Merkt S, Hinke C, Bültmann J, Brandt M, Xie YM. Mechanical response of TiAl6V4 lattice structures manufactured by selective laser melting in quasistatic and dynamic compression tests. J Laser Appl 2014;27(S1):S17006. http://dx.doi.org/10.2351/1.4898835.

[47] Xiao L, Song W. Additively-manufactured functionally graded Ti-6Al-4V lattice structures with high strength under static and dynamic loading: Experiments. Int J Impact Eng 2018;111:255–72. http://dx.doi.org/10.1016/j.ijimpeng.2017.09.018, URL https://www.sciencedirect.com/science/article/pii/S0734743X17304852.

[48] Vrána R, Koutecký T, Červinek O, Zikmund T, Pantělejev L, Kaiser J, et al. Deviations of the SLM produced lattice structures and their influence on mechanical properties. Materials 2022;15(9). http://dx.doi.org/10.3390/ma15093144, URL https://www.mdpi.com/1996-1944/15/9/3144.

[49] Weißmann V, Drescher P, Bader R, Seitz H, Hansmann H, Laufer N. Comparison of single Ti6Al4V struts made using selective laser melting and electron beam melting subject to part orientation. Metals 2017;7(3). http://dx.doi.org/10.3390/met7030091, URL https://www.mdpi.com/2075-4701/7/3/91.

[50] Hossain U, Ghouse S, Nai K, Jeffers JR. Mechanical and morphological properties of additively manufactured SS316l and Ti6Al4V micro-struts as a function of build angle. Addit Manuf 2021;46:102050. http://dx.doi.org/10.1016/j.addma.2021.102050, URL https://www.sciencedirect.com/science/article/pii/S2214860421002153.

[51] Dong Z, Liu Y, Li W, Liang J. Orientation dependency for microstructure, geometric accuracy and mechanical properties of selective laser melting AlSi10Mg lattices. J Alloys Compd 2019;791:490–500. http://dx.doi.org/10.1016/j.jallcom.2019.03.344, URL https://www.sciencedirect.com/science/article/pii/S092583881931182X.

[52] Dallago M, Raghavendra S, Luchin V, Zappini G, Pasini D, Benedetti M. Geometric assessment of lattice materials built via Selective Laser Melting. Mater Today: Proc 2019;7:353–61. http://dx.doi.org/10.1016/j.matpr.2018.11.096, 1st International Conference on Materials, Mimicking, Manufacturing from and for Bio Application (BioM&M), 27-29 June 2018, URL https://www.sciencedirect.com/science/article/pii/S2214785318328554.

[53] Murchio S, Dallago M, Zanini F, Carmignato S, Zappini G, Berto F, et al. Additively manufactured Ti–6Al–4V thin struts via laser powder bed fusion: Effect of building orientation on geometrical accuracy and mechanical properties. J Mech Behav Biomed Mater 2021;119:104495. http://dx.doi.org/10.1016/j.jmbbm.2021.104495, URL https://www.sciencedirect.com/science/article/pii/S1751616121001806.

[54] Wilkinson T, Casata M, Barba D. An alloy-agnostic machine learning framework for process mapping in laser powder bed fusion. Rapid Prototyp J 2024;30(11):302–23.

[55] Schneider C, Rasband WS, Eliceiri KW. NIH Image to ImageJ: 25 years of image analysis. Nature Methods 2012;9:671–5. http://dx.doi.org/10.1038/nmeth.2089.

[56] Miyambo ME, Von Kallon DV, Pandelani T, Reinecke JD. Review of the development of the split hopkinson pressure bar. Procedia CIRP 2023;119:800–8. http://dx.doi.org/10.1016/j.procir.2023.04.010, The 33rd CIRP Design Conference, URL https://www.sciencedirect.com/science/article/pii/S2212827123005826.

[57] Wang P, Xu S, Li Z, Yang J, Zhang C, Zheng H, et al. Experimental investigation on the strain-rate effect and inertia effect of closed-cell aluminum foam subjected to dynamic loading. Mater Sci Eng: A 2015;620:253–61. http://dx.doi.org/10.1016/j.msea.2014.10.026, URL https://www.sciencedirect.com/science/article/pii/S0921509314012696.

[58] Fíla T, Koudelka P, Falta J, Zlámal P, Rada V, Adorna M, et al. Dynamic impact testing of cellular solids and lattice structures: Application of two-sided direct impact hopkinson bar. Int J Impact Eng 2021;148:103767. http://dx.doi.org/10.1016/j.ijimpeng.2020.103767, URL https://www.sciencedirect.com/science/article/pii/S0734743X2030837X.

[59] AlMahri S, Santiago R, Lee D-W, Ramos H, Alabdouli H, Alteneiji M, et al. Evaluation of the dynamic response of triply periodic minimal surfaces subjected to high strain-rate compression. Addit Manuf 2021;46:102220. http://dx.doi.org/10.1016/j.addma.2021.102220, URL https://www.sciencedirect.com/science/article/pii/S2214860421003808.

[60] Jin N, Wang Y, Cheng H, Cheng X, Zhang H. Strain rate and structure dependent behavior of lattice structures of a titanium alloy fabricated by selective laser melting. J Dyn Behav Mater 2022;8(1):57–72. http://dx.doi.org/10.1007/s40870-021-00318-3.

[61] Bregoli C, Mohajerani S, Fiocchi J, Mehrpouya M, Elahinia M, Tuissi A, et al. Impact of surface finishing on Ti6Al4V voronoi additively manufactured structures: Morphology, dimensional deviation, and mechanical behavior. Materials 2024;17(19). http://dx.doi.org/10.3390/ma17194879, URL https://www.mdpi.com/1996-1944/17/19/4879.

[62] Bartolomeu F, Costa M, Alves N, Miranda G, Silva F. Selective Laser Melting of Ti6Al4V sub-millimetric cellular structures: Prediction of dimensional deviations and mechanical performance. J Mech Behav Biomed Mater 2021;113:104123. http://dx.doi.org/10.1016/j.jmbbm.2020.104123, URL https://www.sciencedirect.com/science/article/pii/S1751616120306718.

[63] Cansizoglu O, Harrysson O, Cormier D, West H, Mahale T. Properties of Ti–6Al–4V non-stochastic lattice structures fabricated via electron beam melting. Mater Sci Eng: A 2008;492(1):468–74. http://dx.doi.org/10.1016/j.msea.2008.04.002, URL https://www.sciencedirect.com/science/article/pii/S0921509308003663.

[64] Zhang XZ, Tang HP, Leary M, Song T, Jia L, Qian M. Toward manufacturing quality Ti-6Al-4V lattice struts by Selective Electron Beam Melting (SEBM) for lattice design. JOM 2018;70:1870–6. http://dx.doi.org/10.1007/s11837-018-3030-x.

[65] Tian Y, Ren H, He J, Zha X, Lin K, Zhou M, Xiong Y. Surface roughness improvement of Ti-6Al-4V alloy overhang structures via process optimization for laser-powder bed fusion. J Manuf Process 2024;110:434–46. http://

dx.doi.org/10.1016/j.jmapro.2024.01.008, URL https://www.sciencedirect.com/science/article/pii/S1526612524000094.
[66] Fadida R, Shirizly A, Rittel D. Dynamic tensile response of additively manufactured Ti6Al4V with embedded spherical pores. J Appl Mech 2018;85(4):041004. http://dx.doi.org/10.1115/1.4039048.
[67] Mirone G, Barbagallo R, Giudice F, Di Bella S. Analysis and modelling of tensile and torsional behaviour at different strain rates of Ti6Al4V alloy additive manufactured by electron beam melting (EBM). Mater Sci Eng: A 2020;793:139916. http://dx.doi.org/10.1016/j.msea.2020.139916, URL https://www.sciencedirect.com/science/article/pii/S0921509320309886.
[68] Ran C, Zhou Q, Chen P, Chen Q, Zhang W. Comparative experimental study of the dynamic properties and adiabatic shear susceptibility of titanium alloys. Eur J Mech A Solids 2021;85:104137. http://dx.doi.org/10.1016/j.euromechsol.2020.104137, URL https://www.sciencedirect.com/science/article/pii/S0997753820305258.
[69] Dehgahi S, Pirgazi H, Sanjari M, Alaghmandfard R, Tallon J, Odeshi A, et al. Texture evolution during high strain-rate compressive loading of maraging steels produced by laser powder bed fusion. Mater Charact 2021;178:111266. http://dx.doi.org/10.1016/j.matchar.2021.111266, URL https://www.sciencedirect.com/science/article/pii/S1044580321003880.
[70] Knott J. Fundamentals of fracture mechanics. Butterworth; 1973, URL https://books.google.es/books?id=gXtWq1_eHC8C.
[71] Alabort Martínez C, Barba Cancho D, Reed R, Alabort E. Effect of size on the limit strain of additive manufactured titanium. 2019.
[72] Kouprianoff D, du Preez W. Reducing time and cost of the heat treatment post-processing of additively manufactured Ti6Al4V. Mater Today Commun 2023;35:106186. http://dx.doi.org/10.1016/j.mtcomm.2023.106186, URL https://www.sciencedirect.com/science/article/pii/S2352492823008772.
[73] Waymel RF, Chew HB, Lambros J. Loading orientation effects on the strength anisotropy of additively-manufactured Ti-6Al-4V alloys under dynamic compression. Exp Mech 2019;59(6):829–41. http://dx.doi.org/10.1007/s11340-019-00506-2.
[74] Alaghmandfard R, Dharmendra C, Odeshi A, Mohammadi M. Deformation and fracture behavior of electron beam melted ti-6al-4v under high strain rate impacts. 2019, p. 75–82. http://dx.doi.org/10.7449/2019/MST_2019_75_82, URL https://www.scopus.com/inward/record.uri?eid=2-s2.0-85075331585&doi=10.7449%2f2019%2fMST_2019_75_82&partnerID=40&md5=e1aceb63d96eeecf968fdbb1fd3e0a4b,
[75] Alaghmandfard R, Chalasani D, Odeshi A, Mohammadi M. Activated slip and twin systems in electron beam melted ti-6al-4v subjected to elevated and high strain rate dynamic deformations. Mater Charact 2021;172:110866. http://dx.doi.org/10.1016/j.matchar.2020.110866, URL https://www.sciencedirect.com/science/article/pii/S1044580320323378.
[76] Nemat-Nasser S, Guo W-G, Nesterenko VF, Indrakanti S, Gu Y-B. Dynamic response of conventional and hot isostatically pressed ti–6al–4V alloys: experiments and modeling. Mech Mater 2001;33(8):425–39. http://dx.doi.org/10.1016/S0167-6636(01)00063-1, URL https://www.sciencedirect.com/science/article/pii/S0167663601000631.
[77] Zhao X, Li S, Zhang M, Liu Y, Sercombe TB, Wang S, et al. Comparison of the microstructures and mechanical properties of Ti–6Al–4V fabricated by selective laser melting and electron beam melting. Mater Des 2016;95:21–31. http://dx.doi.org/10.1016/j.matdes.2015.12.135, URL https://www.sciencedirect.com/science/article/pii/S0264127515309928.
[78] Antonysamy A, Meyer J, Prangnell P. Effect of build geometry on the β-grain structure and texture in additive manufacture of Ti6Al4V by selective electron beam melting. Mater Charact 2013;84:153–68. http://dx.doi.org/10.1016/j.matchar.2013.07.012, URL https://www.sciencedirect.com/science/article/pii/S1044580313002131.
[79] Zhang C, Liu F, Wang H. Effect of the prior-β grain boundaries on mechanical behavior of Ti6Al4V alloy processed by laser directed energy deposition. Mater Sci Eng: A 2022;848:143389. http://dx.doi.org/10.1016/j.msea.2022.143389, URL https://www.sciencedirect.com/science/article/pii/S0921509322007821.
[80] Alaghmandfard R, Dharmendra C, Odeshi A, Mohammadi M. Dynamic mechanical properties and failure characteristics of electron beam melted Ti-6Al-4V under high strain rate impact loadings. Mater Sci Eng: A 2020;793:139794. http://dx.doi.org/10.1016/j.msea.2020.139794, URL https://www.sciencedirect.com/science/article/pii/S0921509320308686.
[81] Zhang JS, Deng Y, Liu H, Tang YT, Lui A, Grant PS, et al. Orientation matters: Assessing the cyclic deformation behaviour of laser powder bed fusion Ti-6Al-4V. Mater Des 2024;248:113485. http://dx.doi.org/10.1016/j.matdes.2024.113485, URL https://www.sciencedirect.com/science/article/pii/S0264127524008608.
[82] Dallago M, Winiarski B, Zanini F, Carmignato S, Benedetti M. On the effect of geometrical imperfections and defects on the fatigue strength of cellular lattice structures additively manufactured via Selective Laser Melting. Int J Fatigue 2019;124:348–60. http://dx.doi.org/10.1016/j.ijfatigue.2019.03.019, URL https://www.sciencedirect.com/science/article/pii/S0142112319300957.
[83] Roach AM, White BC, Garland A, Jared BH, Carroll JD, Boyce BL. Size-dependent stochastic tensile properties in additively manufactured 316L stainless steel. Addit Manuf 2020;32:101090. http://dx.doi.org/10.1016/j.addma.2020.101090, URL https://www.sciencedirect.com/science/article/pii/S2214860419315738.
[84] Vazquez-Fernandez NI, Soares GC, Smith JL, Seidt JD, Isakov M, Gilat A, et al. Adiabatic heating of austenitic stainless steels at different strain rates. J Dyn Behav Mater 2019;5(3):221–9. http://dx.doi.org/10.1007/s40870-019-00204-z.
[85] Li P-H, Guo W-G, Huang W-D, Su Y, Lin X, Yuan K-B. Thermomechanical response of 3D laser-deposited Ti–6Al–4V alloy over a wide range of strain rates and temperatures. Mater Sci Eng: A 2015;647:34–42. http://dx.doi.org/10.1016/j.msea.2015.08.043, URL https://www.sciencedirect.com/science/article/pii/S0921509315302914.
[86] Benedetti M, Fontanari V, Bandini M, Zanini F, Carmignato S. Low- and high-cycle fatigue resistance of Ti-6Al-4V ELI additively manufactured via selective laser melting: Mean stress and defect sensitivity. Int J Fatigue 2018;107:96–109. http://dx.doi.org/10.1016/j.ijfatigue.2017.10.021, URL https://www.sciencedirect.com/science/article/pii/S014211231730419X.
[87] Benedetti M, du Plessis A, Ritchie R, Dallago M, Razavi N, Berto F. Architected cellular materials: A review on their mechanical properties towards fatigue-tolerant design and fabrication. Mater Sci Eng: R: Rep 2021;144:100606. http://dx.doi.org/10.1016/j.mser.2021.100606, URL https://www.sciencedirect.com/science/article/pii/S0927796X21000012.
[88] Maconachie T, Leary M, Tran P, Harris J, Liu Q, Lu G, et al. The effect of topology on the quasi-static and dynamic behaviour of SLM AlSi10Mg lattice structures. Int J Adv Manuf Technol 2022;118(11):4085–104. http://dx.doi.org/10.1007/s00170-021-08203-y.
[89] Rashed M, Ashraf M, Mines R, Hazell PJ. Metallic microlattice materials: A current state of the art on manufacturing, mechanical properties and applications. Mater Des 2016;95:518–33. http://dx.doi.org/10.1016/j.matdes.2016.01.146, URL https://www.sciencedirect.com/science/article/pii/S0264127516301447.
[90] Ashby MF. The properties of foams and lattices. Philos Trans R Soc A: Math Phys Eng Sci 2006;364:15–30. http://dx.doi.org/10.1098/rsta.2005.1678.
[91] Jin N, Wang F, Wang Y, Zhang B, Cheng H, Zhang H. Failure and energy absorption characteristics of four lattice structures under dynamic loading. Mater Des 2019;169:107655. http://dx.doi.org/10.1016/j.matdes.2019.107655, URL https://www.sciencedirect.com/science/article/pii/S0264127519300929.
[92] Forés-Garriga A, Gómez-Gras G, Pérez MA. Mechanical performance of additively manufactured lightweight cellular solids: Influence of cell pattern and relative density on the printing time and compression behavior. Mater Des 2022;215:110474. http://dx.doi.org/10.1016/j.matdes.2022.110474, URL https://www.sciencedirect.com/science/article/pii/S0264127522000958.
[93] Tancogne-Dejean T, Mohr D. Stiffness and specific energy absorption of additively-manufactured metallic BCC metamaterials composed of tapered beams. Int J Mech Sci 2018;141:101–16. http://dx.doi.org/10.1016/j.ijmecsci.2018.03.027, URL https://www.sciencedirect.com/science/article/pii/S0020740318304855.
[94] Li Y, Jiang D, Zhao R, Wang X, Wang L, Zhang L-C. High mechanical performance of lattice structures fabricated by additive manufacturing. Metals 2024;14(10). http://dx.doi.org/10.3390/met14101165, URL https://www.mdpi.com/2075-4701/14/10/1165.
[95] Tan PJ, Harrigan JJ, Reid SR. Inertia effects in uniaxial dynamic compression of a closed cell aluminium alloy foam. Mater Sci Technol 2002;18(5):480–8. http://dx.doi.org/10.1179/026708302225002092.
[96] Zhao M, Liu F, Fu G, Zhang DZ, Zhang T, Zhou H. Improved mechanical properties and energy absorption of BCC lattice structures with triply periodic minimal surfaces fabricated by SLM. Materials 2018;11(12). http://dx.doi.org/10.3390/ma11122411, URL https://www.mdpi.com/1996-1944/11/12/2411.
[97] Gorny B, Niendorf T, Lackmann J, Thoene M, Troester T, Maier H. In situ characterization of the deformation and failure behavior of non-stochastic porous structures processed by selective laser melting. Mater Sci Eng: A 2011;528(27):7962–7. http://dx.doi.org/10.1016/j.msea.2011.07.026, URL https://www.sciencedirect.com/science/article/pii/S0921509311008057.
[98] Mines R, Tsopanos S, Shen Y, Hasan R, McKown S. Drop weight impact behaviour of sandwich panels with metallic micro lattice cores. Int J Impact Eng 2013;60:120–32. http://dx.doi.org/10.1016/j.ijimpeng.2013.04.007, URL https://www.sciencedirect.com/science/article/pii/S0734743X13000912.